Geophysical Journal International

Geophys. J. Int. (2010) **183,** 1579–1595 doi: 10.1111/j.1365-246X.2010.04816.x

Diversity of fault zone damage and trapping structures in the Parkfield section of the San Andreas Fault from comprehensive analysis of near fault seismograms

Michael A. Lewis* and Yehuda Ben-Zion

Department of Earth Sciences, University of Southern California, Los Angeles, CA 90089–0740*, USA. E-mail: m5lewis@ucsd.edu*

Accepted 2010 September 16. Received 2010 August 17; in original form 2010 January 14

SUMMARY

We perform comprehensive analyses of trapped waves and signals of damaged fault zone rocks associated with time delays of body waves along the Parkfield section of the San Andreas Fault (SAF). Waveforms generated by thousands of earthquakes and recorded by near fault stations in several permanent and temporary deployments are examined, with attention to the possible influence of a lithology contrast across the fault on signals of the low velocity damage zone. Clear candidate trapped waves are identified at only three stations, MMNB and two of the other near fault stations (FLIP and PIES) further to the NW. Clear candidate trapped waves are not seen at any of the near fault stations to the SE of MMNB. The locations of the events generating good candidate trapped waves at MMNB and the other two stations are not distributed broadly in space, but clustered in a small number of locations. Moreover, events that generate clear candidate trapped waves at one station do not typically generate trapped waves at the other two stations. These observations imply that the damage zone is highly variable along strike and that a coherent connected waveguide does not exist for distances along strike larger than at most 3–5 km (the distance between stations). Synthetic waveform fits for observed trapped waves at stations MMNB and FLIP indicate that the most likely parameters of the trapping structures at these locations are widths of about 150 m, depths of about 3 km, velocity reductions of 30–40 per cent, and Q values of 10–40. Synthetic calculations of trapped waves demonstrate that if there is a contrast of seismic velocity across the fault, the trapped waves are delayed relative to the *S* wave arrival. Trapped waves at station MMNB, and to a lesser extent also at stations FLIP and PIES in the NW section, show this characteristic. This suggests a lithology contrast in the top few km at these locations, in agreement with results from tomography and studies of head waves in the Parkfield area. At several mini across-fault arrays, where trapped waves are not observed, a low velocity damage zone is detected from the delay in the arrival time of body wave phases relative to a nearby off-fault station. The observed delay of the *S* wave is greater than the *P* wave delay, consistent with the existence of a damage zone with Poisson ratio of about 0.33. The observations of time delays without trapped waves indicate that parts of the damage zone are insufficiently coherent to generate trapped waves. A broader damage zone may exist in the region between the SAF and the South West Fracture Zone. The results highlight the diversity of damage structures along the ∼40 km of the SAF examined in this study, and imply that fault imaging based on data at single sites does not necessarily apply to a larger section.

Key words: Earthquake dynamics; Body waves; Interface waves; Guided waves; Rheology and friction of fault zones; Continental tectonics: strike-slip and transform.

1 INTRODUCTION

Large fault zone (FZ) structures with damaged rocks and material discontinuity (bimaterial) interfaces can generate several seismic signals that can be used for high-resolution imaging of the subsurface FZ structure. High crack density may produce prominent scattering (e.g. Benites *et al.* 1992; Nishigami 2000; Revenaugh 2000), non-linear wave propagation effects (e.g. Sawazaki *et al.* 2006; Rubinstein *et al.* 2007; Wu *et al.* 2009), increasing attenuation (e.g. Jongmans & Malin 1995; Korneev *et al.* 2003) and overall reduction of seismic velocities (e.g. Thurber *et al.* 2006; Li

*Now at: Marine Physical Laboratory, Scripps Institution of Oceanography, La Jolla, California 92093–0238.

et al. 2007). A preferred crack orientation can lead to anisotropy of seismic velocity and attenuation (e.g. Cochran *et al.* 2003; Peng & Ben-Zion 2004; Liu *et al.* 2005; Boness & Zoback 2006). A fault consisting of a bimaterial interface between different rock bodies can produce head waves that spend much of their propagation path along the bimaterial interface (e.g. Ben-Zion 1989, 1990; Ben-Zion & Malin 1991; Lewis *et al.* 2007; Zhao *et al.* 2010). A spatially coherent zone of damaged rocks may generate trapped waves associated with constructive interference of critically reflected phases within the low velocity FZ layer (e.g. Ben-Zion & Aki 1990; Li *et al.* 1990, 1994; Ben-Zion *et al.* 2003; Haberland *et al.* 2003).

Most previous imaging studies based on analyses of trapped waves agree that the trapping structures in large FZs consist of 100–200 m wide layers of damaged rocks characterized by 30–50 per cent velocity reduction and strong attenuation ($Q \approx$ 10–40) of *S* waves. However, there is considerable debate on the depth extent and along-strike coherency of the seismic trapping zones. A number of studies argued that seismic trapping structures along various FZs extend continuously to depths of 10–20 km and that the trapping structures are continuous along strike for several tens of kilometres (e.g. Li & Leary 1990; Li *et al.* 1994; Li & Vernon 2001; Mizuno & Nishigami 2006). These studies have generally relied on forward waveform and traveltime modelling, dispersion analysis and related techniques, but they did not perform formal data inversions that can quantify the likelihood and uncertainties of the inferred model parameters.

Ben-Zion (1998) demonstrated with analytical model calculations that trapped waves are subjected to significant trade-offs, and that nearly identical waveforms can be generated with many combinations of the width, spatial extent, velocity reduction and other parameters of the FZ damage layer. Similar trade-offs exist in the dispersion properties of trapped waves (Peng *et al.* 2003). Igel *et al.* (1997, 2002) and Jahnke *et al.* (2002) showed with numerical simulations that trapped waves average out various internal variations of the FZ structure with correlation length smaller than the overall FZ width. These include gradual changes of properties across the fault, vertical velocity gradients, internal scatterers, and other small-scale heterogeneities. Observed trapped waves can thus be used to derive effective average waveguide properties of FZ segments over which they propagate. However, the strong trade-offs among basic model parameters can lead to significant uncertainties in the interpretation of results. A quantitative analysis of trapped waves should consider volumes in parameter-space that produce the same results, and include information on the likelihood of different sets of derived parameters.

Several observational analyses of trapped waves using quantitative waveform inversions that explore large volumes in parameter space concluded that the trapping structures are generally limited to the top 3–5 km of the crust (Ben-Zion *et al.* 2003; Peng *et al.* 2003; Lewis *et al.* 2005). The results were established by calculating fitness values of synthetic seismograms for ∼10,000 sets of model parameters and using the fitness values to estimate the most probable sets of model parameters. These studies also concluded that the trapping structures are typically not coherent along-strike for tens of kilometres. Mamada *et al.* (2004) performed detailed analyses of data recorded by a subsurface seismometer array near the Mozumi–Sukenobu FZ in Japan and highlighted the existence of strong along-strike structural discontinuities. Michael & Ben-Zion (1998) and Korneev *et al.* (2003) examined large data sets in the Parkfield section of the San Andreas Fault (SAF) and pointed out that clear trapped waves are produced only by events that sample a relatively small section of the fault.

In the present paper, we perform a comprehensive analysis of trapped waves and time delays of body wave arrivals in large waveform data sets recorded by several seismic networks along the Parkfield section of the SAF. In Section 2, we describe briefly the study area and the various employed data sets. In Section 3, we discuss the different signals and procedures used in the data analyses. Synthetic calculations in Section 3 show that the form of FZ trapped waves depends on whether or not there is an overall velocity contrast across the fault. The existence of a velocity contrast across the fault can have important effects on various aspects of earthquake dynamics and the generated ground motion (e.g. Ben-Zion & Huang 2002; Shi & Ben-Zion 2006; Ampuero & Ben-Zion 2008; Brietzke *et al.* 2009). The analyses results, described in Section 4, highlight the diversity of FZ damage structures seen in different portions of the ∼40-km-long examined section of the SAF. Clear trapped waves are observed only at station MMNB and in weaker forms at two other stations further to the NE, and have at all three locations the expected signature of a velocity contrast across the SAF. The trapped waves are generated at restricted FZ sections, with dimensions less than the 3–5 km distance between the stations where they are observed, in agreement with the earlier findings of Michael & Ben-Zion (1998) and Korneev *et al.* (2003). Clear-trapped waves are not observed at any of the near fault stations to the SE of MMNB; however, the presence of a low velocity zone is observed in the delay of the *P* and *S* wave arrivals. The performed systematic analyses indicate that the SAF at Parkfield has a complex internal structure, with several seismic trapping zones of limited depth and along-strike extent, interspaced with less coherent damage zone layers and structural discontinuities.

2 TECTONIC ENVIRONMENT OF THE PARKFIELD SECTION OF THE SAF AND USED DATA SETS

The Parkfield section of the SAF spans the transition between the creeping segment of the fault to the northwest and the locked segment to the southeast, which last broke in the great 1857 Fort Tejon earthquake (Sieh 1978). The rock types in this section are generally characterized by Gabilan granite on the SW side of the fault and slower Franciscan rock on the NE side (e.g. Lees & Malin 1990; Thurber *et al.* 2006). The San Andreas system between Middle Mountain (MM) and Gold Hill (GH) is expressed (Fig. 1) as two principle surface traces (Brown *et al.* 1967; Rymer *et al.* 2006): the main SAF and the Southwest Fracture Zone (SWFZ). The SAF surface trace shows a right-stepping offset across the Cholame Valley south of GH. This offset is thought to be the north end of the locked segment that ruptured in the 1857 event and to be responsible for bounding the southern rupture extents of the M6 Parkfield earthquakes (Lindh & Boore 1981). The aftershocks of the 2004 Parkfield earthquake concentrate along the same locations associated with the pre-2004 seismicity and form a linear trend that is directly underneath the SWFZ rather than the main SAF (Eberhart-Phillips & Michael 1993; Simpson *et al.* 2004; Waldhauser *et al.* 2004; Thurber *et al.* 2006). The seismicity appears to connect to the creeping and locked sections of the SAF without obvious bends, suggesting that the SAF is expressed as a single planar fault at seismogenic depth. However, the lack of shallow seismicity makes it difficult to relate the simple fault outlined by the seismicity with the multiple surface traces of the fault. At least seven earthquakes of ∼M6 occurred on the Parkfield segment since 1857, with the most recent on 2004 September 28 (Bakun *et al.* 2005). The

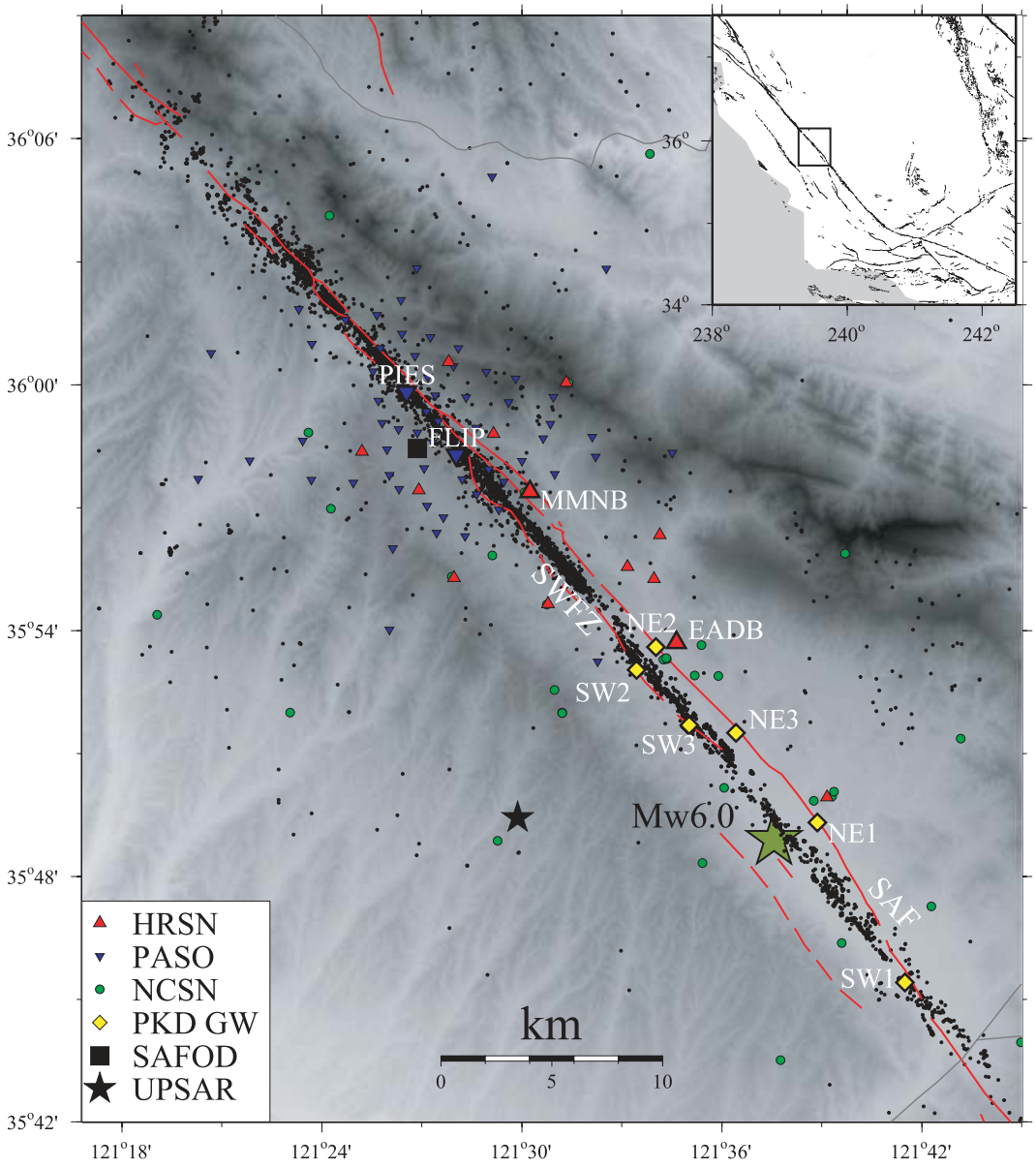

Figure 1. Map of the Parkfield section of the San Andreas fault (SAF) with an insert that shows the map location in central California. The Shading represents the topography and the lines (red in the main map and black in the insert) indicate major faults. The earthquakes from the relocated catalogue of Thurber *et al.* (2006) are shown as black circles and the epicentre of the 2004 M6 Parkfield event is highlighted as a green star. The employed stations of different networks used in the study are marked by the symbols indicated at the left bottom corner. The data that are discussed primarily in this study are associated with the stations denoted by larger symbols and names.

quasi-periodicity of the previous six events led to the deployment of many seismic and other instruments as part of the Parkfield Earthquake Prediction Experiment (Bakun & Lindh 1985).

Several groups have performed 3-D tomography in the Parkfield area (Lees & Malin 1990; Michelini & McEvilly 1991; Eberhart-Phillips & Michael 1993; Thurber *et al.* 2003, 2006). Their results indicate that there is a step in seismic velocity across the main SAF that extends throughout the seismogenic zone, with the across-fault contrast ranging from a few to about 10 per cent. This existence of a sharp interface between two differing materials is also demonstrated clearly by observations of FZ head waves at a number of stations on the NE (slow) side of the fault (Ben-Zion & Malin 1991; Ben-Zion *et al.* 1992). Zhao *et al.* (2010) used large numbers of head wave observations to map variations of velocity contrast and found values of about 5–10 per cent north of High Resolution Seismic Network (HRSN) station MMNB that decrease to 0–2 per cent near GH. Observations of FZ trapped waves indicate that the fault is also associated with a low velocity damage zone. Trapped waves have been reported at two HRSN stations (Li *et al.* 1990; Korneev *et al.* 2003), in the SAFOD (San Andreas Fault Observatory at Depth) borehole following the *S* as well as the *P* arrivals (Ellsworth *et al.* 2007; Li & Malin 2008) and at temporary arrays of instruments from microearthquakes and explosions (Li *et al.* 1997).

The seismograms analysed in this study are from (Fig. 1) near fault stations within the HRSN operated by the Berkeley Seismological Laboratory, along with two temporary deployments: the Parkfield Area Seismic Observatory (PASO) Network (Thurber *et al.* 2003) and the 2004 Parkfield guided wave (PKD GW) experiment

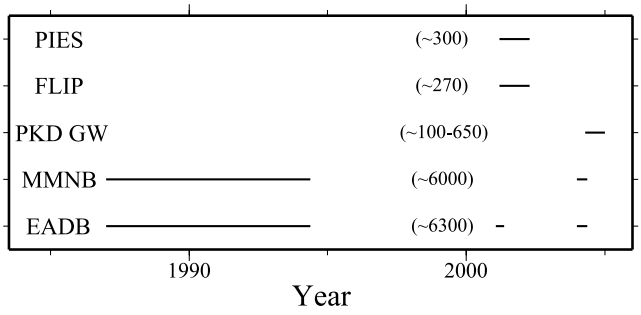

Figure 2. A summary of time intervals (black lines) of employed data at the PIES and FLIP stations from the PASO network, EADB and MMNB stations from the HRSN network, and the mini arrays of the PKD GW experiment. The approximate numbers of employed events at the various stations are indicated in parentheses.

(Michael *et al.* 2005). In the PKD GW deployment stations were arranged as mini across-fault arrays of up to three stations. One station is directly on the fault trace of either the SAF or SWFZ, as well as this can be determined, while a second and sometimes third instrument are placed ∼100–200 m from the central FZ station to the NE and SE. Most surface instruments are 1 Hz L4C or 2 Hz L22 short-period velocity sensors with a sampling rate of 100 s^{-1}. In the PASO network, 29 stations are equipped with Guralp 40T broad-band instruments. The HRSN 2 Hz or 4.5 Hz short-period sensors are deployed in 100–300 m deep boreholes and have a sampling rate of 250 s^{-1}. The hypocenter locations and origin times of earthquakes are obtained from the relocated catalogue of Thurber *et al.* (2006). The differing times of the various deployments means that events are not necessarily common between the different sets of stations. The time intervals and approximate numbers of events recorded at the various FZ stations utilized in this study are shown in Fig. 2.

3 EMPLOYED SIGNALS

We examine the spatial extent of the damage zone around the fault using two techniques, trapped waves and the reduction of seismic velocity at stations within the FZ compared to those outside. The locations where these phenomena are observed, and the strength with which they occur, provide information on how significantly the velocity is reduced in the fault damage zone and how continuous along the strike of the fault it is. FZ trapped or guided waves have been used to characterize low velocity damage zones associated with several fault and rupture zones, including the Parkfield section of the SAF (Li *et al.* 1990; Li *et al.* 1997; Michael & Ben-Zion 1998; Korneev *et al.* 2003, Ellsworth *et al.* 2007), the San Jacinto fault (Li & Vernon 2001; Lewis *et al.* 2005), the rupture zone of the 1992 Landers earthquake (Li *et al.* 1994; Peng *et al.* 2003), an inactive fault in central Italy (Rovelli *et al.* 2002) and the Karadere–Duzce branch of the North Anatolian fault (Ben-Zion *et al.* 2003). These studies were done with a single or a small number of arrays of instruments across the fault and some studies presented results associated with only a limited number or subset of events.

Aside from the ambiguity in the waveform fitting that arises from the strong trade-offs between several key FZ parameters (Ben-Zion 1998), the use of limited stations and events can lead to an overly simplified view of the FZ structure. Such studies do not account for the many events recorded at FZ stations that do not generate trapped waves, or the fact that at some stations trapped waves are not observed at all. In this paper, we focus on the spatial variations of FZ properties at different near fault stations, using many different events at each station to characterize the heterogeneity of the low velocity damage zones in the Parkfield section of the SAF. The presence and quality of trapped waves and the later arrival of seismic phases in FZ stations are used to determine the variations of properties of the damaged FZ layers. Numerical simulations of trapped waves (Igel *et al.* 1997; Igel *et al.* 2002; Jahnke *et al.* 2002; Fohrmann *et al.* 2004) indicate that structural heterogeneities with length scales smaller than the average width of the trapping zone do not affect the trapped waves. However, larger scale heterogeneities destroy the waveguide and lead to a low velocity zone that does not produce trapped waves. These studies also showed that energy can become trapped in a coherent waveguide, if the event is within the low velocity layer or if it is outside and below it. Thus the observation of trapped waves indicates that a relatively coherent damage zone exists between the station and the source location; however, the damage zone does not necessarily extend continuously all the way downward from the station to the source. The existence of FZ damage is also expected to delay the arrival times of the *P* and *S* waves for source-receiver configurations for which the seismic waves have to propagate through the damaged FZ layer (Li *et al.* 2007). This effect does not require the same coherence of the damage zone as is necessary for it to act as a waveguide that produces trapped waves.

3.1 Trapped waves

The constructive interference patterns of critically reflected phases travelling within a spatially persistent and sufficiently uniform low velocity FZ layer are generally termed FZ trapped or guided waves (e.g. Ben-Zion & Aki 1990; Li & Leary 1990; Ben-Zion 1998). As a result of the way they are generated, the amplitude, arrival time, duration and frequency content of the trapped waves depend strongly on the properties of the FZ layer. Hence, trapped waves can provide high-resolution information on the average geometrical and seismic properties of the FZ waveguide section in which they propagate.

Figs 3(a) and (c) show synthetic velocity waveforms with trapped waves generated in a structure consisting of a vertical low velocity layer between two identical quarter-spaces. The red lines mark the *S* wave arrivals and immediately following these are FZ trapped waves marked by thick black overbars. The waveforms are calculated using the 2-D analytical solution of Ben-Zion & Aki (1990) and Ben-Zion (1998). The motion is generated by an SH line dislocation with a unit step source-time function located at the interface between the FZ layer and the left quarter-space. The media *S* wave velocities are indicated in the figure and the *Q* values outside and inside the FZ are 200 and 20, respectively. In Fig. 3(a) the station is located 50m from a 100m wide damage zone in the left quarter-space while in Fig. 3(c) it is 50m from the damage zone in the right quarter-space. The results illustrate how the number of cycles, amplitude and dispersion of trapped waves all increase with propagation distance within the waveguide. As shown in other studies, the trapped waves are predominant in the vertical and fault-parallel components and their amplitude decreases rapidly with increasing distance of the recording station from the fault (e.g. Ben-Zion & Aki 1990; Li & Leary 1990; Igel *et al.* 1997, 2002). These unique characteristics differentiate trapped waves from any other amplification effects and signals in the waveforms that may be caused by various other propagation, site and instrumental effects.

As mentioned in Section 2, imaging studies of the Parkfield region indicate that in general the SAF in this area is a boundary

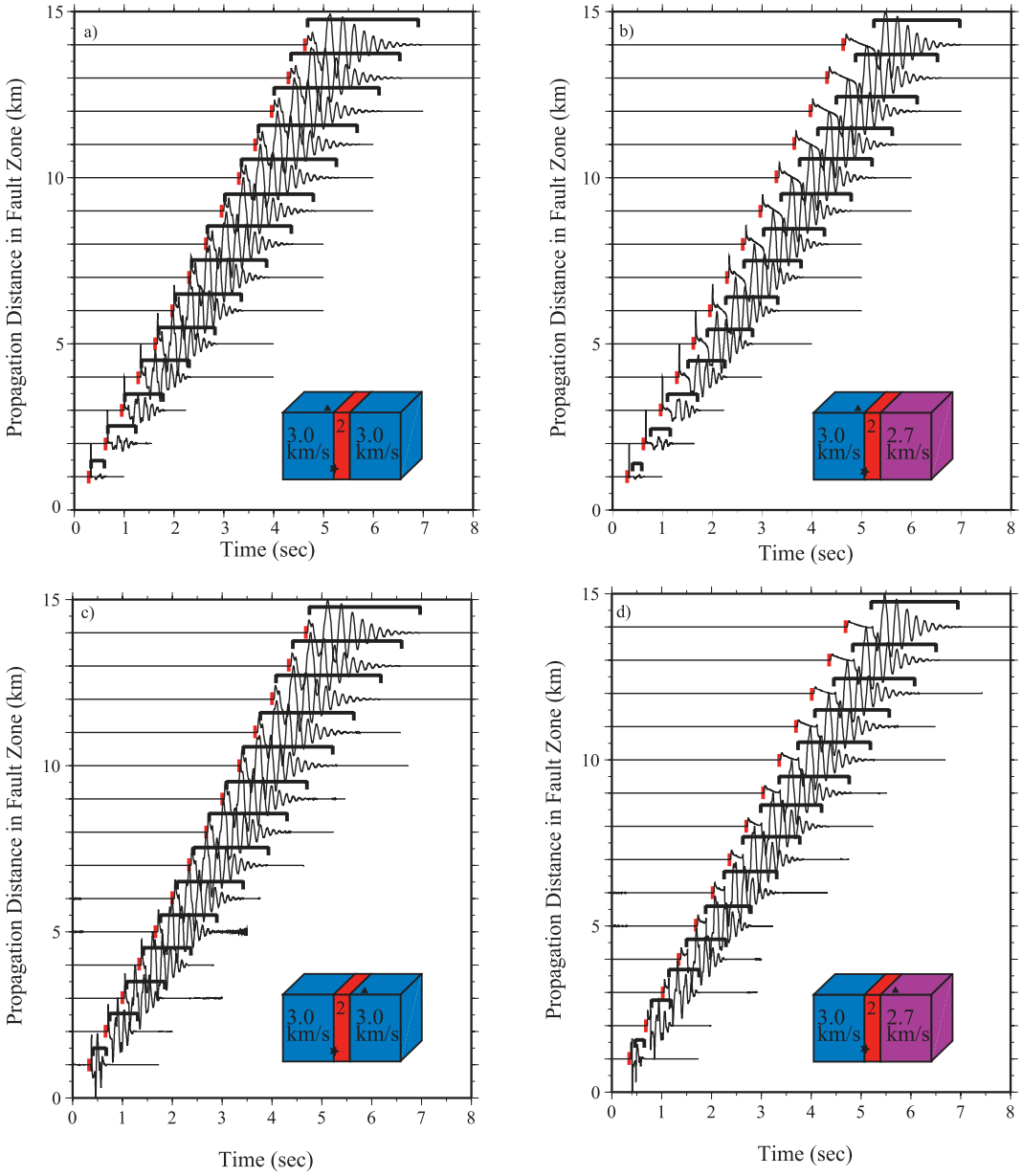

Figure 3. Synthetic velocity waveforms at increasing propagation distances generated by the 2-D analytical solution of Ben-Zion & Aki (1990) and Ben-Zion (1998) for a model consisting of a vertical low velocity layer between two quarter-spaces. Each seismogram is normalized to its maximum amplitude. In (a) and (c) the two bounding quarter-spaces are identical while in (b) and (d) they have different properties. The cartoons in the bottom right corners show the employed model configurations and S velocities, with the stars and triangles indicating the locations of sources and receivers, respectively. The used Q values are 20 in the fault zone (FZ) layer and 200 outside. The vertical red lines show the S wave arrivals and the generated trapped waves are bracketed by horizontal black bars.

between rocks with different velocities. To examine how the properties of trapped waves are modified by the existence of an overall velocity contrast across the fault, Figs 3(b) and (d) display synthetic waveforms generated for a FZ structure consisting of a vertical low velocity layer between two different quarter-spaces. All other properties of the model apart from the velocities are the same as in Figs 3(a) and (c). A comparison with Figs 3(a) and (c) indicates that the velocity contrast across the FZ leads to a separation between the *S* arrival and the start of the trapped waves and the separation increases with increasing propagation distance in the FZ layer. These properties are the same for near fault stations on either side of the fault. The same holds for stations located within the FZ layer, although in such cases the amplitudes of the trapped waves are larger. The clear differences in the waveform properties between the direct *S* wave and start of the trapped waves group can be used to distinguish between situations where the low velocity FZ layer is between similar and dissimilar solids.

3.2 Time delays of phases

Li *et al.* (2007) modelled waveforms generated by events within or just outside a low velocity FZ layer and observed at an array of stations across the fault. They demonstrated with synthetic waveforms that the arrival times of *P* and *S* waves vary across the fault as a result of delays produced by the FZ layer. The *P* and *S* wave

Table 1. Calculated *P* and *S* wave velocities for examples of elastic constants given in the text for undamaged and damaged rocks. The velocity reduction and velocity ratios between the two examples of rock types are also given.

	V_s (m s^{-1})	V_p (m s^{-1})	V_p/V_s
Undamaged	2981.42	5163.98	1.732
Damaged	2418.25	4800.81	1.985
Percent reduction	18.89	7.03	

velocities in a given elastic medium are given by

$$V_p = \sqrt{\frac{E(1-\upsilon)}{\rho(1-2\upsilon)(1+\upsilon)}} \tag{1}$$

and

$$V_p = \sqrt{\frac{E}{2\rho(1+\upsilon)}}, \tag{2}$$

where E, ρ and υ are, respectively, the Young modulus, mass density and Poisson ratio. Dividing these results, the velocity ratio is

$$\frac{V_p}{V_s} = \sqrt{\frac{2(1-\upsilon)}{1-2\upsilon}}. \tag{3}$$

The reduced *P* and *S* wave velocities in the FZ result primarily from rock damage associated with higher crack density along with some mineral alteration. Taking a mass density of 2500 kg m^{-3}, undamaged elastic constants of $\upsilon = 0.25$, E = 60 GPa and damaged elastic constants of $\upsilon = 0.33$ and $E = 42$ GPa, give basic expectations that are summarized in Table 1.

Figs 4(a) and (b) illustrate with velocity and displacement synthetic seismograms the expected phase delays for *S* waves produced by propagation through a low velocity FZ layer. The model consists of a 100 m wide FZ layer with *S* wave velocity of the damaged rock in Table 1 and $Q = 20$, between two similar quarter-spaces with *S* wave velocity of the undamaged rock in Table 1 and $Q = 200$. As before, the source is at the interface between the FZ layer and left quarter-space. The synthetic waveforms are generated for pairs of stations at equal distances from the source, but in each case one path crossing the low velocity zone and the other path going through the undamaged quarter-space. The *S* arrival times are marked and the later arrivals at the station with phases travelling through the FZ layer (green seismograms) are evident. The results show clearly that for closely-spaced stations across the FZ, with nearly the same hypocentral distances, there should be phase delays for configurations where the waves cross the FZ and that the delay in the *S* wave arrival would be greater than for the *P* wave. These characteristic expressions of the FZ in the seismograms do not require the same spatial coherency and relative homogeneity of the damage zone that is necessary to generate and sustain guided trapped waves.

3.3 Analysis procedure and example results

We use several criteria to identify trapped waves, as they have a specific set of properties that distinguish them from other amplifications or modifications of the ground motions, which may be produced by various other sources. Candidate trapped waves must follow the direct body wave, have relatively low frequencies, be at least somewhat dispersive and exist predominantly in the vertical and fault parallel components of ground motion (Ben-Zion & Aki 1990). The amplitudes of the trapped waves should be higher the closer the station is to the fault and decay rapidly with increasing normal distance from the fault. If there is no velocity contrast across the FZ, the trapped waves should follow directly and have comparable or larger amplitude than the body waves (Fig. 3a). If the propagation distance in the FZ is larger than about 5 km, the trapped waves should have clear dispersion (Ben-Zion 1998; Peng *et al.* 2003). If there is a velocity contrast across the fault we would expect to see a separation between the direct *S* and trapped waves (Fig. 3b).

Before conducting detailed analyses, all sets of waveforms in the various used data sets (Fig. 1) are rotated to a fault parallel, fault perpendicular and vertical coordinate system. The azimuth of the fault, to which the components are rotated, is estimated from fitting a

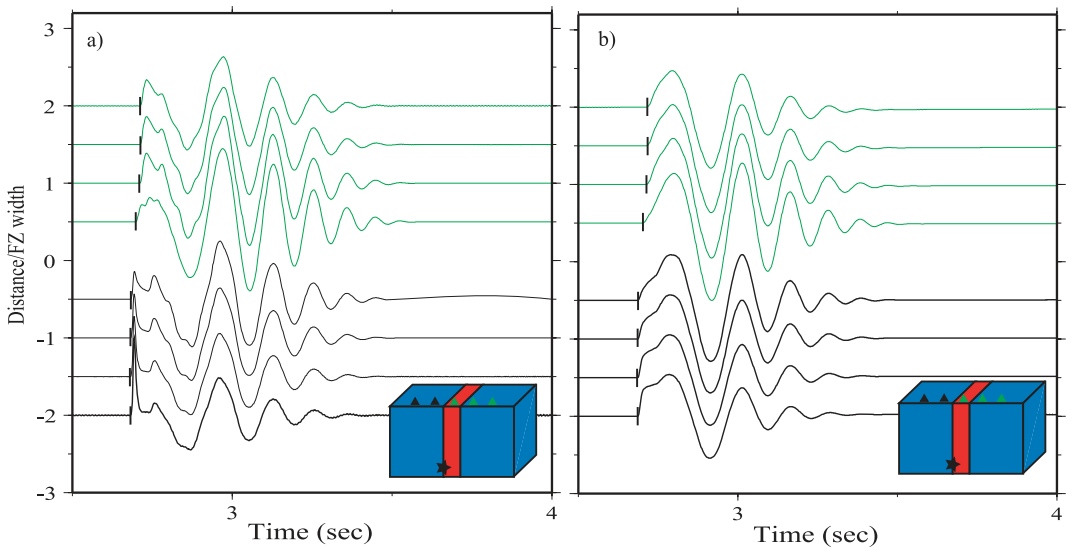

Figure 4. (a) Synthetic velocity seismograms generated with the same model as in Fig. 3 using the media velocities from Table 1. The FZ layer is characterized by $Q = 20$ and the velocity of the damaged rock, while the bounding quarter-spaces are characterized by $Q = 200$ and the velocity of the undamaged rock. The cartoon in the bottom right corner indicates the locations of the source and receivers. The green colour denotes stations and seismograms with propagation paths through the low velocity FZ layer, while the black colour denotes stations and seismograms with propagation paths through undamaged rocks. The vertical black lines denote the S wave arrivals. (b) Same as in (a) for displacement seismograms.

line to the highly localized epicentre locations. Waveforms recorded at stations close to the fault from each of the networks are examined for the strength of the characteristics of trapped waves, and whenever possible the waveforms of the near fault station are compared to a second nearby station further from the fault. This is done to increase the likelihood that the identified features are associated with the FZ and are not due to source or other propagation and site effects. The waveforms are then assigned a quality rating between 1 and 4 based on how prominent the trapped waves characteristics are. Quality 1 implies the highest likelihood of trapped waves, quality 2 means the waveforms have the characteristics of trapped waves but they are less pronounced, quality 3 means there are only some of the features of trapped waves (e.g. amplification in only one component or there is no dispersion despite a long duration of amplification) and quality 4 means none of the trapped waves attributes were present or were obscured by a poor signal to noise ratio. Only waveforms with quality 1 and 2 are likely to be associated with trapped waves. Quality 3 waveforms may represent some propagation-site effects related to the FZ, but they do not have one or more of the key features that are expected for trapped waves (Ben-Zion & Aki 1990).

Fig. 5 shows examples of 3-compoenent velocity seismograms recorded at the HRSN station MMNB with quality 1 and 2 of trapped

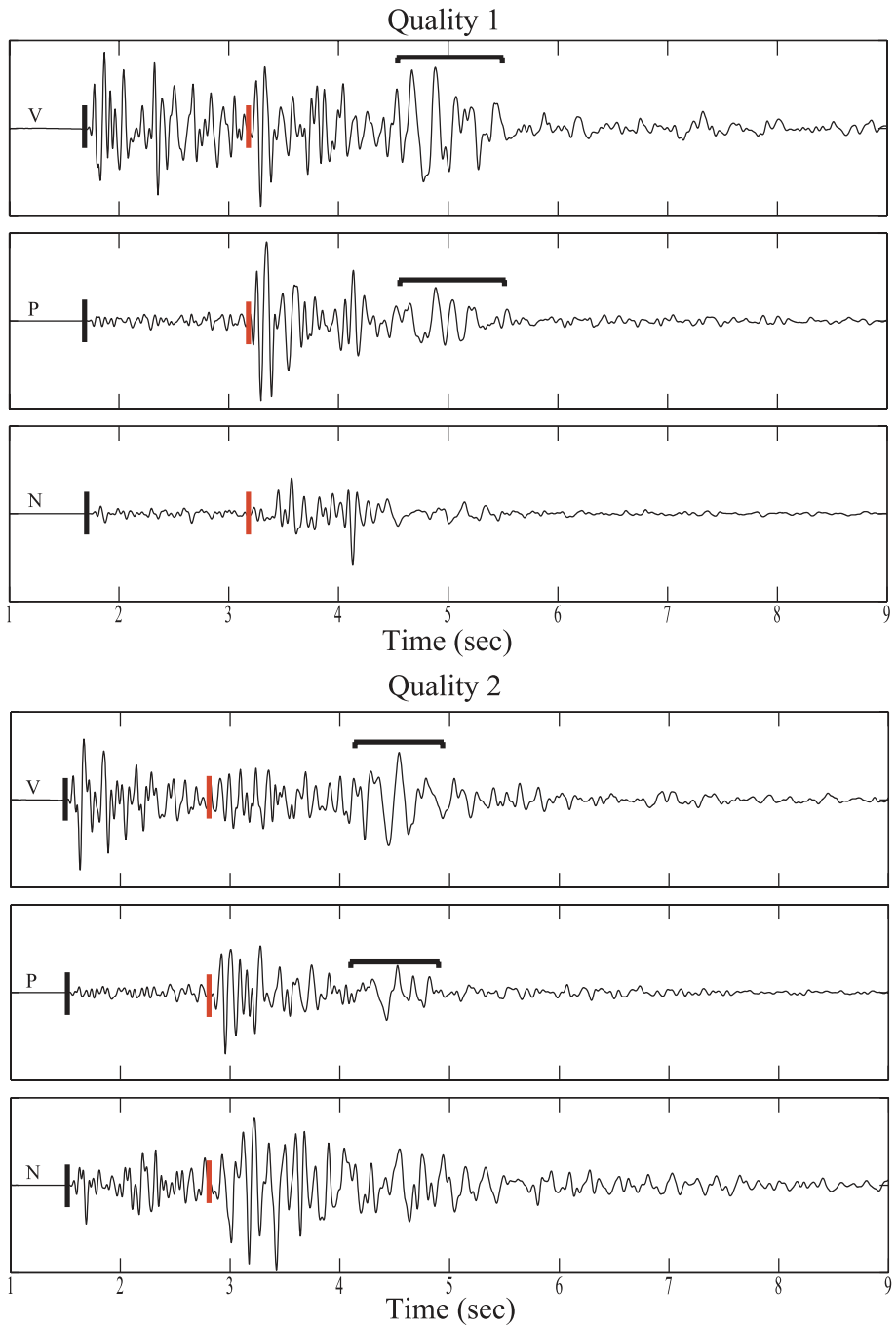

Figure 5. Observed three component seismograms (vertical – V, fault parallel – P, fault normal – N) illustrating quality 1 trapped waves (top) and quality 2 (bottom) data. The vertical black and red bars show the picks for the *P* and *S* wave arrivals, while the estimated time of the trapped waves are bracketed by horizontal black bars.

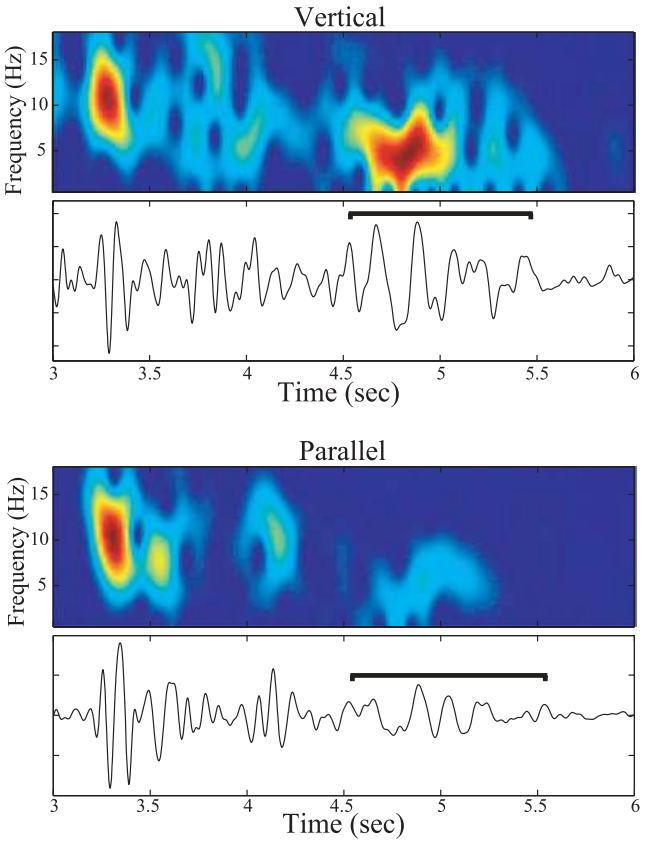

Figure 6. Spectrogram and the corresponding seismogram from the portion following the *S* wave of the V and P components of the quality 1 data in Fig. 5. The estimated time of the trapped waves (same as in Fig. 5) are bracketed by horizontal black bars.

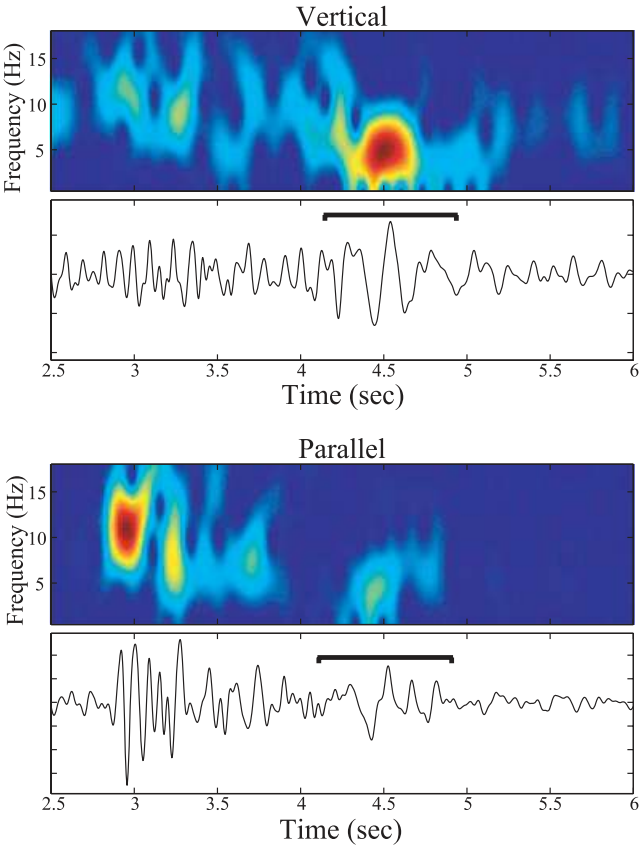

Figure 7. Same as Fig. 6 for the quality 2 data of trapped waves from the lower panel in Fig. 5.

waves. Figs 6 and 7 give the amplitudes of different frequencies as a function of time for the vertical and fault-parallel seismograms for the two quality levels of Fig. 5. The candidate-trapped waves (thick overbars) are clearly visible following the *S* wave (red vertical bar) and the spectrograms confirm that they have lower frequencies than the *S* waves (Figs 6 and 7). There is no obvious dispersion, but this is not unexpected when the duration of the trapped waves is short. These two features of the trapped waves together imply a short propagation distance within the damage zone. The candidate trapped waves in Fig. 5 have a clear separation from and similar amplitude to the *S* wave, which are expected characteristics for situations with an overall velocity contrast across the fault and relatively short propagation distance within the waveguide (Section 3.1).

With each set of seismograms assigned a quality of candidate trapped waves as illustrated above, the distribution of the events, which do and do not generate candidate trapped waves at each station can be mapped. Fig. 8 exhibits the distribution of the events identified to produce candidate trapped waves at station MMNB, with the size and colour of the symbols representing the quality of trapped waves. The identification and classification of trapped waves was done by careful (time consuming) visual inspection of thousands of observed seismograms (and many corresponding spectrograms) at MMNB, with some subsets of data examined independently by two–three people to ensure robustness of the overall results. The black triangle in Fig. 8 represents approximately the area identified by Korneev *et al.* (2003) to be associated with a relatively low Q value and the production of trapped waves. The area enclosed by the circle was highlighted by Michael & Ben-Zion (1998) as a limited region with events generating trapped waves at station MMNB. The comprehensive analysis summarized by Fig. 8 indicates that the events producing clear trapped waves at MMNB are confined to a limited region, which coincides generally with the limited regions identified by Korneev *et al.* (2003) and Michael & Ben-Zion (1998).

To further quantify the seismic properties of the FZ waveguide, we perform synthetic waveform modelling on sets of observed FZ trapped waves using the 2-D analytical solution of Ben-Zion and Aki (1990) and Ben-Zion (1998). The employed model configuration consists of a single vertical FZ layer between two potentially different quarter-spaces and the source is at the interface between the FZ and the left quarter-space. Previous studies using a similar model (without an overall velocity contrast across the fault) produced good waveform fits for trapped waves observed along the Karadere–Duzce branch of the North Anatolian fault (Ben-Zion *et al.* 2003), the rupture zone of the 1992 Landers earthquake (Peng *et al.* 2003), the San Jacinto FZ (Lewis *et al.* 2005) and other locations (Haberland *et al.* 2003; Mizuno *et al.* 2004). To quantitatively account for the trade-offs in model parameters discussed in Section 1, we model observed sets of FZ trapped waves using a genetic inversion algorithm (GIA) that employs the 2-D analytical solution as a forward kernel (Michael & Ben-Zion 1998). The free parameters in the inversion are the *S* wave velocities of the FZ and host rocks, the *S* wave attenuation coefficient of the FZ material, the width and propagation distance inside the FZ layer, the source position and the centre of the FZ layer. To reduce the number of parameters, the attenuation coefficients of the host rocks are fixed at 1000 and the location of the station is fixed at its appropriate

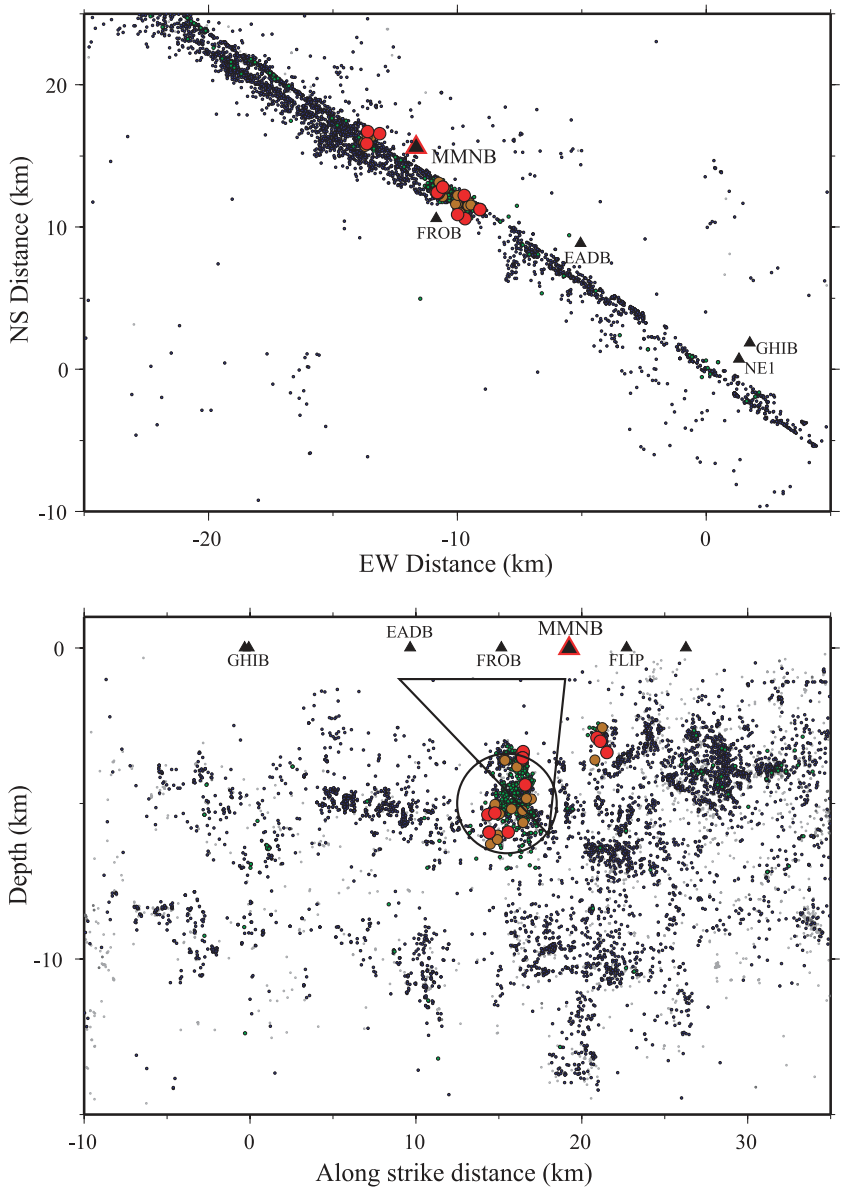

Figure 8. A summary of quality of observed trapped waves generated by ongoing seismicity and recorded at station MMNB. The top panel gives a map view with EW and NS distances centred at the epicentre of the 2004 M6 earthquake. The bottom panel presents results projected on the fault plane. The colour and size of each symbol correspond to the quality of trapped waves in the following order: best quality (quality 1) red circles, second best (2) orange circles, third best (3) green circles, lowest quality (4) blue circles. The large circle denotes the limited area identified by Michael & Ben-Zion (1998) as producing clear trapped waves at MMNB, while the triangle marks the limited region identified by Korneev *et al.* (2003) as producing clear trapped waves.

position normal to the fault trace. Prior to the inversion, the seismograms are pre-processed by removing the instrument response and converting the fault-parallel seismograms into displacement. We also convolve the seismograms with $t^{-1/2}$ to obtain the equivalent 2-D line-source seismograms (e.g. Igel *et al.* 2002; Ben-Zion *et al.* 2003). Additional details on the method can be found in Ben-Zion *et al.* (2003).

As mentioned in Section 3.2, the lack of observed trapped waves at a FZ station implies the absence of a coherent waveguide. However, a discontinuous or diffuse damage zone is expected to delay seismic phases propagating through it, with the delay of the *S* wave being greater than that of the *P* wave. The mini arrays of the PKD GW deployment with their central station located on the fault and up to two nearby (∼100 m) off fault stations are well suited for analysis of the expected delay effects. All the waveforms recorded by the mini arrays are first examined to determine which ones have sufficiently impulsive and clear *P* and *S* wave onsets to accurately obtain arrival times. Based on the signal to noise ratio associated with the body wave arrivals, we create a subset of high quality data for further analysis of delay times. Within this subset of high signal to noise waveforms, the *P* and *S* wave arrival times are picked on each of the three components and at each of the stations within the across-fault mini arrays. If there is no clear *S* wave arrival on the vertical component or no clear *P* on the horizontal components, these data are not used. Example velocity seismograms produced by two events and recorded at the two operating stations in the NE1 array are shown in Fig. 9. The arrivals at the FZ station (NE1C) are clearly delayed relative to the nearby off-fault station, and the delays

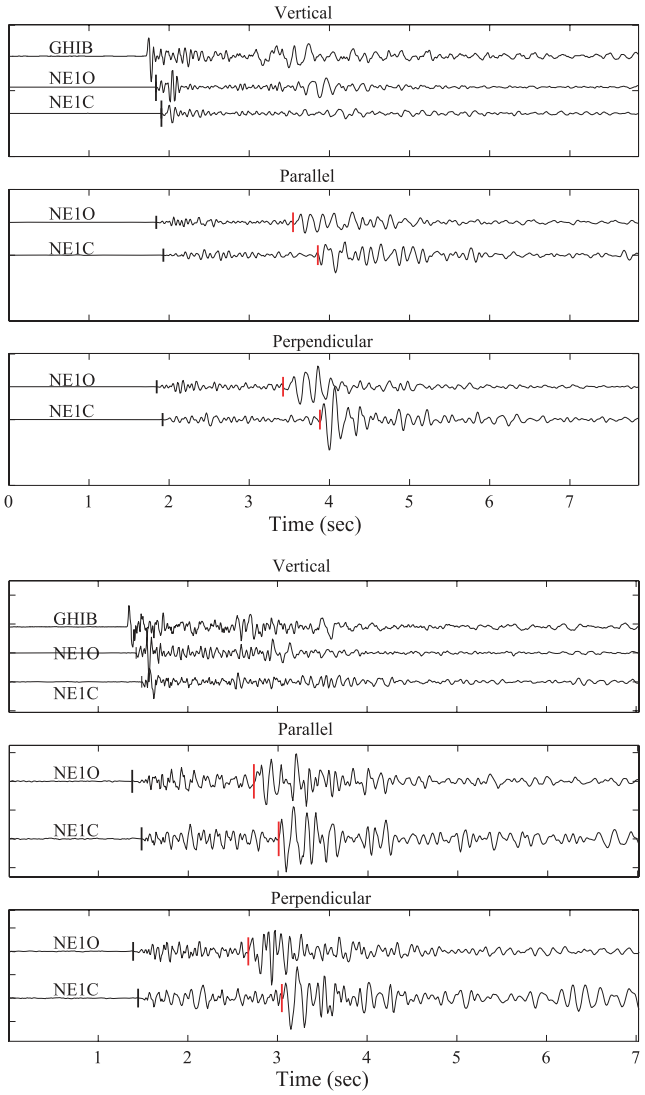

Figure 9. Example sets of 3-component velocity seismograms from two events (top and bottom panels) recorded at two station of the NE1 array of the PKD GW deployment (NE1C in the centre of the FZ and station NE1O about 250 m NE of the fault). For the vertical component, the data of nearby HRSN station GHIB is also shown. The vertical black and red lines mark the *P* and *S* wave arrivals, respectively.

associated with the *S* waves are greater for these two events than those associated with the *P* waves. The magnitude of arrival time differences from different events and at different stations should reflect the properties of the low velocity FZ layer between the employed sources and receivers.

4 COMPREHENSIVE ANALYSIS RESULTS

Fig. 10 shows the detailed distribution of candidate trapped waves at four stations, two from the HRSN network (MMNB and EADB) and two from the PASO network (PIES and FLIP). Stars and diamonds represent quality 1 and 2 candidate trapped waves, while the lower qualities 3 and 4 are indicated by the smaller circles. The colour of the symbol for the event corresponds to the station it was recorded at. In some cases the same event may have a symbol for multiple stations and have a different quality rating at each of them. As discussed in the context of Fig. 8, the results were obtained by careful examinations of thousands of observed seismograms (and many corresponding spectrograms), with some subsets of data examined independently by two–three people to ensure robustness of the overall results. The waveforms at FZ stations PIES and FLIP were examined along with data at 10 other on and near fault stations from the PASO network. Clear high-quality candidate trapped waves are identified only at MMNB, PIES and FLIP. Quality 1 or 2 candidate trapped waves were not seen at the HRSN stations GHIB and EADB, at any of the PKD GW stations, or at the other nine near fault stations of the PASO deployment. While GHIB and EADB are somewhat further from the fault, which might explain a lack of observed trapped waves energy, multiple other stations are close to the fault. This holds particularly for the PKD GW stations which are located on the main SAF or SWFZ traces.

The quality 1 and 2 events are all within about 5–10 km along strike from the station where they are recorded and they are not evenly distributed in space but rather tend to appear as clusters in certain localized regions. This can be seen clearly in the cross section in Fig. 10 where the symbols representing the highest quality candidates for trapped waves for each station appear in distinct localized regions. For two different neighbouring near fault stations, the events producing the highest quality trapped waves are not the same ones nor are they necessarily in the same area. There are no overlapping symbols of quality 1 for the same event at different stations in Fig. 10. These observations imply that whether or not trapped waves are generated is not solely a function of where a station is placed or where events occur but a combination of the two. This is not what would be expected for a single coherent waveguide that is continuous for a considerable distance along the fault. The results imply instead trapping structures with limited depth and along-strike dimensions (estimated below based on waveform modelling) that are sufficiently coherent only to generated trapped waves from events in some specific locations near the recording stations. Some quality 1 and 2 events have crossing paths for stations MMNB and FLIP, as well as FLIP and PIES, but none produce trapped waves at any pair of stations. A trapping structure along a deep fault section underneath both stations MMNB and FLIP (or FLIP and PIES) that simply diverges near the surface will produce trapped waves from some events at both stations (e.g. fig 15 of Jahnke *et al.* 2002). Since this is not observed, the detailed analysis results of Fig. 10 indicate the existence of a complex FZ structure with multiple disconnected shallow waveguide sections that are continuous along the fault for less than the distance between the stations (5–10 km).

Fig. 11 shows examples of synthetic waveform fits for data recorded at MMNB and FLIP along with the fitness values calculated by the GIA for different FZ parameters. The inversion is run to fit simultaneously a number of quality 1 events at each station, producing best fitting models to six events at MMNB (Figs 11a and b) and five events at FLIP (Figs 11c and d). The two stations are considered separately because they are on different parts of the fault (about 3 km apart) and as seen in Fig. 10 clear trapped waves at MMNB and FLIP are generated by different subsets of events. The fitness for a given set of parameters is defined as $(1+C)/2$, where C is the cross-correlation coefficient between the employed sets of observed and synthetic waveforms. The thin curves in Figs 11(b) and (d) give probability density functions for the various model parameters, calculated by summing the fitness values of the final 2000 inversion iterations and normalizing the results to have unit sums. The synthetic waveform fits were generated using the best fitting parameters associated with the highest fitness values during 10 000 iterations. As seen visually and indicated by the high fitness

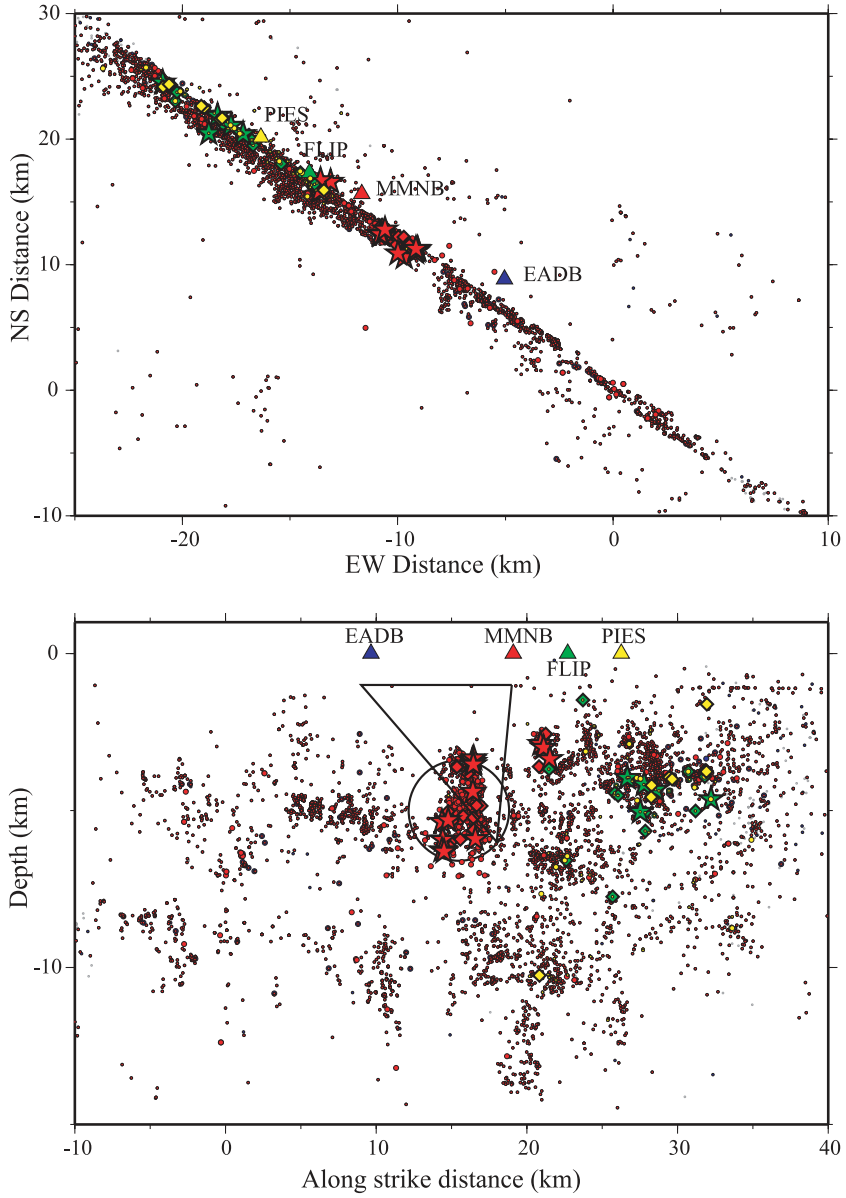

Figure 10. A summary of assigned quality of candidate trapped waves generated by ongoing seismicity and recorded at four stations (triangles). The top panel gives a map view with EW and NS distances centred at the epicentre of the 2004 M6 earthquake. The bottom panel presents results projected on the fault plane. The size and shape of each symbol correspond to the quality of candidate trapped waves in the following order: best quality (quality 1) large stars, second best (2) medium diamonds, third best (3) small circles, lowest quality (4) very small circles. The colours of each symbol correspond to the stations at which it was recorded. The same event may have different symbols for different stations if it produced data at the different stations. The large circle denotes the limited area identified by Michael & Ben-Zion (1998) as producing clear trapped waves at MMNB, while the triangle marks the limited region identified by Korneev *et al.* (2003) as producing clear trapped waves.

values between synthetic and observed seismograms, the model results fit well the main characteristics of the recorded trapped waves.

The ranges of parameters with relatively high fitness values provide estimates for the uncertainties associated with the best fitting parameters. From these inversions, the most likely parameters of the structures generating the trapped waves at these locations are FZ widths of 140–160 m, reductions of shear wave velocity from the lower velocity bounding block to the FZ of 30–40 per cent, Q values in the FZ of 10–40 and depths of the trapping structure of 2–4 km. The latter values are based on propagation distances within the trapping structures of 3–5 km, which include some along-strike components. As discussed previously there are strong trades-offs between the different parameters in the modelling of trapped waves (Ben-Zion 1998) and these values are not intended to give the exact characteristics of the FZ properties. They do, however, provide the most likely ranges of parameters and indicate again that the trapped waves propagate within local structures that extend only a few kilometres around the stations, as the total propagation distance returned by the inversion never exceeds 6 km. Similar to the distribution of the high quality trapped waves, the propagation distances from the inversion results imply variable damage zones along the strike of the fault. The differences between the most likely inversion parameters associated with the data recorded by stations MMNB and FLIP reflect the diversity of the damage FZ structures, but may also be related partially to the fact that MMNB is a 220 m deep borehole

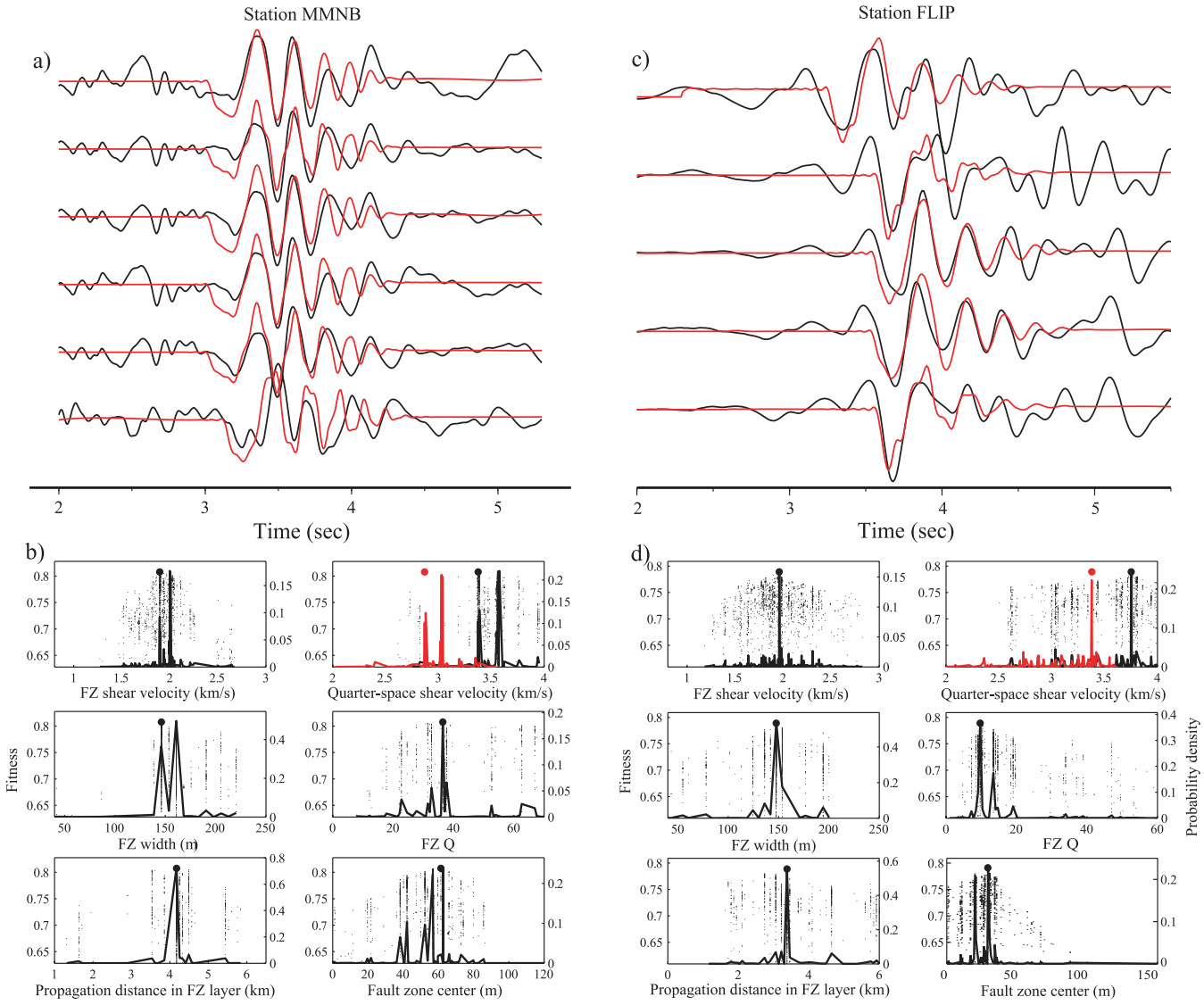

Figure 11. (a) Synthetic (red) waveform fits to fault-parallel displacement seismograms (black) recorded at station MMNB. (b) Fitness values (dots) associated with different FZ parameters tested by the genetic inversion algorithm. The model parameters associated with the highest fitness values (solid circles) were used to generate the synthetic waveforms in (a). The black curves give probability density functions for the various model parameters. The highest fitness values and probability density functions of the two quarter-spaces on the opposite sides of the fault are represented by red and black colors. (c) Synthetic (red) waveform fits for fault-parallel displacement seismograms (lines) recorded at station FLIP. (d) Same as (b) for the synthetic fits associated with seismograms recorded at FLIP.

station while FLIP is a surface station. Differences between results associated with observed trapped waves at borehole and surface stations were also noted by Mizuno & Nishigami (2006) in the context of the Nojima FZ in Japan.

Modelling additional sets of observed quality 1 trapped waves produces very similar results, since the waveforms of the recorded quality 1 trapped waves are very similar. This is because all the generating events are located in relatively tight clusters below the trapping structures (Fig. 10) and the observed trapped waves average out (over the generated wavelengths) internal variations of geometry and material properties of the localized overriding waveguides (e.g. Igel *et al.* 1997, 2002; Jahnke *et al.* 2002; Fohrmann *et al.* 2004). It may perhaps be informative to model sets of quality 2 trapped waves, which are somewhat different than the quality 1 waveforms, although the obtained information is bound to be less reliable than that associated with the quality 1 waveforms. Fig. 12 presents results of modelling sets of waveforms with quality 2 trapped waves recorded at stations MMNB (left) and FLIP (right). The observed trapped waves in Fig. 12 do not appear with casual inspection very different than the quality 1 phases in Fig. 11. It should be remembered, however, that the quality of the trapped waves cannot be judged only from examination of these fault parallel components. All the expected features of trapped waves discussed earlier (relatively high amplitude, relatively low frequencies, at least some dispersion and ground motion predominantly in the vertical and fault parallel components) are considered in the quality assignments. The fitness values associated with the inversions of the quality 2 trapped waves are shown in Figs 12(b) and (d). The best fitting (circles) and local maxima of the probability density functions (thin curves) of the FZ velocity contrast, width, Q, centre and propagation distance in the trapping structure are similar to those obtained by modelling quality 1 waveforms (Fig. 11).

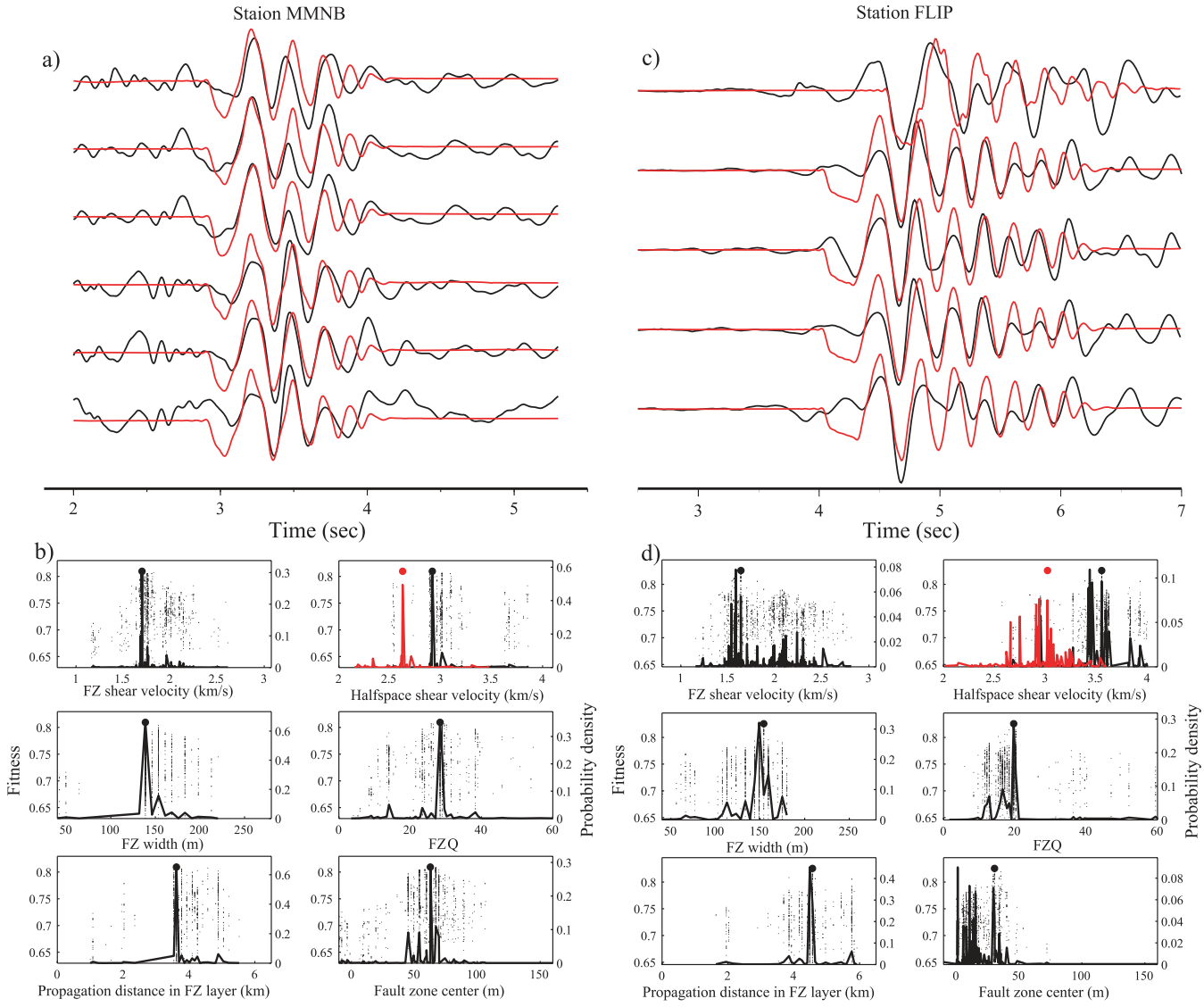

Figure 12. (a) Similar to Fig. 11(a) for quality 2 trapped waves recorded at MMNB. (b) Similar to Fig. 11(b) for the analysed quality 2 trapped waves. (c) Similar to Fig. 11(c) for quality 2 trapped waves recorded at FLIP. (d) Same as (b) for the synthetic fits associated with seismograms recorded at FLIP.

Fig. 13 summarizes the observed time differences between the *S* and *P* wave arrival times at the central FZ and other stations of the various mini-arrays of the PKD GW deployment. As discussed in Section 3.2, propagation through a low velocity FZ layer is expected to lead to later phase arrivals, with the effect being larger for the *S* wave. For each of the selected events the arrival times at the off-fault stations are subtracted from the arrival time of the central FZ station. Positive values in Fig. 13 imply that the FZ station has a later arrival than the off-fault station, while negative values mean the opposite. At some of the PKD GW mini arrays there are only two stations while at others there are three (one on the fault trace and two off the fault on either side). In many cases the *S* wave arrival cannot be determined at all or is associated with larger uncertainty than that of the *P* arrival. This is expected as the *S* onset is within the *P* wave coda and it leads to larger scatter of time differences compared with those associated with the *P* phases.

The mini-array NE1 has larger and more consistent delay times than those seen at NE2 and all but one of the values have the same sign (Fig. 13a). The data in Fig. 13(a) also show the expected pattern of a more significant time delay in the *S* wave compared to the *P* wave. The time delay observations are consistent with the existence of a zone of lower velocity damaged rocks under the centre station in mini array NE1. However, the lack of observed trapped waves at that station implies that the low velocity zone is not sufficiently coherent for the generation of FZ guided waves. At the mini array NE2 the arrival differences between the central station and the station to the NE of the fault is slightly positive (Fig. 13b), but the fault station has arrival times that are slightly earlier than those at the station to the SW (Fig. 13f). In both cases, however, the time delays are very small, there is lack of moveout with propagation distance and no correlation between the *P* and *S* wave arrivals differences. Examining the overall pattern of all the mini arrays, the slowest arrivals occur at the stations between the SWFZ and SAF (Figs 13f–i), as they all produce negative values in the arrival time differences, while arrivals at central FZ stations are slower than those outside this region (Figs 13a–e). The results suggest the existence of a broad low velocity damage zone between the SWFZ and SAF at these locations, rather than more localized damaged zones centred under either of the fault traces. This might explain the lack of observed trapped waves at the fault stations of

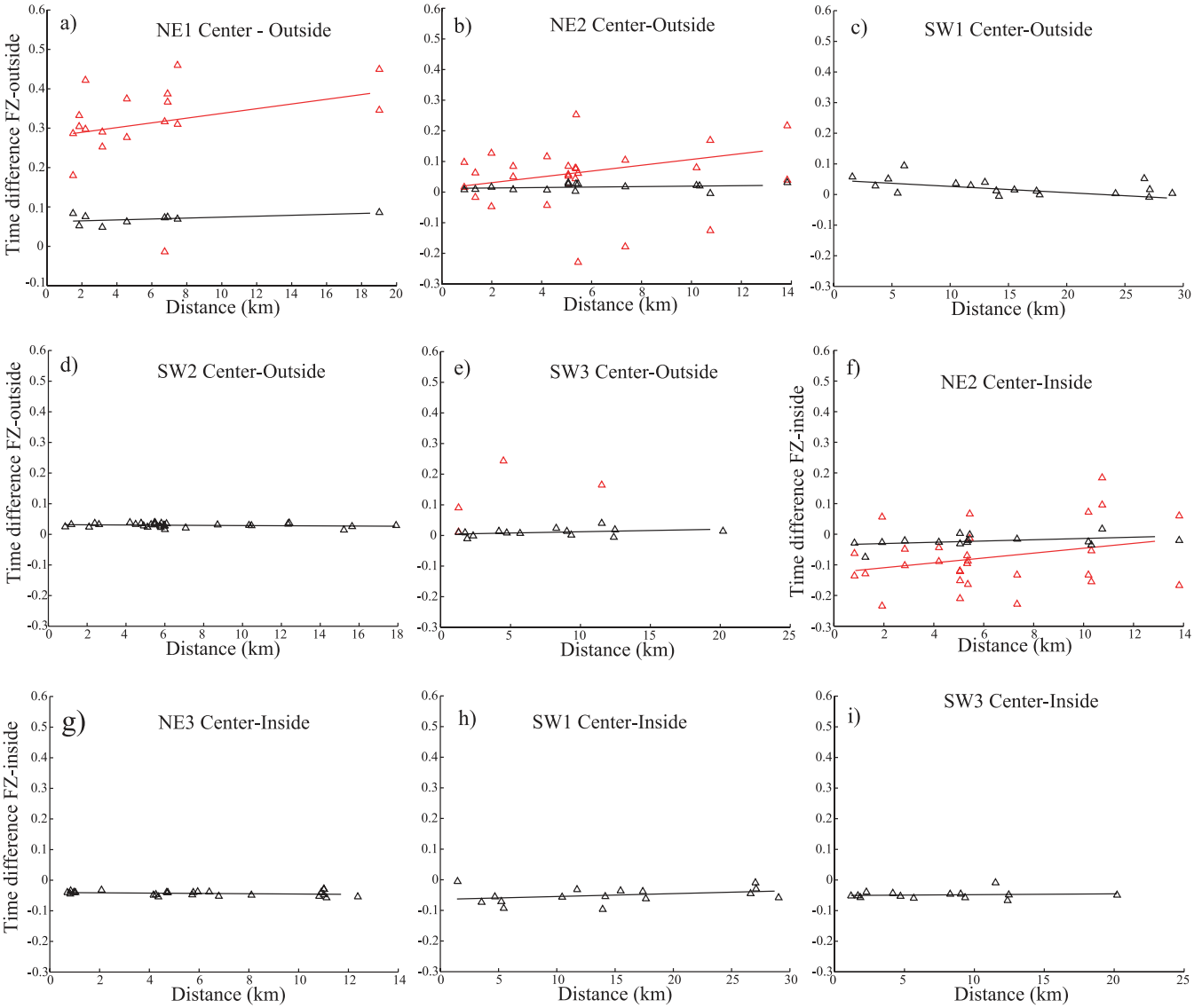

Figure 13. (a) Time difference between body wave arrivals at a central FZ station and off fault stations to the NE or SW. The central FZ stations are on the surface trace of the SAF (NE1, NE2 and NE3) or the SWFZ (SW1, SW2 and SW3). The off fault stations are either between the two faults (inside) or away from the trace in the other direction (outside). Black and red symbols indicate time differences between *P* and *S* wave arrivals, respectively. The lines are least-squares fit to the data. (a)–(e) The arrival time at the central station minus the time at the station outside the fault zone. (f)–(i) The arrival time at the central station minus the time at the station between the SWFZ and SAF.

the mini arrays or other FZ stations near the SAF south of station MMNB. The time delays analysis for the mini-array NE2 may mean that there is no significant damage zone underneath the FZ station in that array, or that all three stations are situated in a very broad damage zone so there is no delay between the different stations. In either case the structure around the NE2 mini array is different than that associated with the other PKD GW stations. All these results highlight again the diversity of the damage structures along the Parkfield section of the SAF.

5 DISCUSSION

In the last 20 years various studies used FZ trapped waves to characterize the internal structure of large fault and earthquake rupture zones (e.g. Li & Leary 1990; Li *et al.* 1994; Rovelli *et al.* 2002; Ben-Zion *et al.* 2003; Haberland *et al.* 2003; Mamada *et al.* 2004; Wang *et al.* 2009). The presence of trapped waves implies a uniform or smoothly varying continuous tabular zone of damage in a region between the recording stations and the generating events (e.g. Ben-Zion & Aki 1990; Fohrmann *et al.* 2004; Wu *et al.* 2008). In contrast, the lack of trapped waves implies that the FZ is too heterogeneous or disjointed between the events and stations to generate or to record any generated trapped waves (e.g. Igel *et al.* 1997, 2002; Jahnke *et al.* 2002). Our comprehensive analysis of large seismic waveform data sets along the Parkfield section of the SAF indicates that trapped waves are not observed at most near fault stations. Clear-trapped waves are observed only at stations MMNB and FLIP (Figs 8 and 10). The observed trapped waves at these stations have signatures of an overall velocity contrast across the fault, in agreement with tomographic images (e.g. Lees & Malin 1990; Michelini & McEvilly 1991; Thurber *et al.* 2006) and analysis of FZ head waves (Ben-Zion & Malin 1991; Ben-Zion *et al.* 1992; Zhao *et al.* 2010) near and to the NW of station MMNB.

The quality of trapped waves in station PIES is considerably below those at stations FLIP and MMNB and the quality of trapped waves in EADS and all other examined stations is lower still. The results also indicate that at stations where clear-trapped waves are observed, they are produced only by events that are clustered into a few locations. This implies that for the majority of the paths between the events and stations the damage zone is not sufficiently coherent and homogenous to act as a seismic waveguide. However, effects of the damage zone can still be observed at some instruments by the delay of phase arrivals that travel through the low velocity FZ material. This is seen to different degrees at stations of the PKD GW mini-arrays, most clearly at NE1 and least clearly at NE2 (Figs 9 and 13). The observed phase delays for the *S* waves at the mini-array NE1 are larger than for the *P* wave. This is consistent with a relatively high Poisson's ratio of 0.33 (Table 1), which is expected for damaged rocks (e.g. Jaeger & Cook 1979; Mavko *et al.* 1998; Hamiel *et al.* 2004). The entire set of observed time delays suggests collectively that there may be a broad low velocity zone between the SAF and SWFZ in the region covered by the PKD GW mini-arrays (SE of the HRSN station EADS).

We infer that stations MMNB and FLIP (and to a lesser extent also PIES), where good candidates trapped waves are observed, are underlain by slivers of relatively-uniform damage zones that act as local seismic waveguides. These zones must have a limited spatial extent as they only trap energy from clusters of events in certain locations that are within a few kilometres of the recording stations. Sets of waveforms with clear trapped waves at stations MMNB and FLIP are fitted (Figs 11 and 12) using the 2-D analytical solution of Ben-Zion & Aki (1990) and the GIA of Michael & Ben-Zion (1998). The relative broad regions with good fitness values in Figs 11 and 12 illustrate that it is possible to obtain good waveform fits with many sets of model parameters. These results highlight the need for inversions of the type done here and related earlier works (e.g. Ben-Zion *et al.* 2003; Peng *et al.* 2003; Lewis *et al.* 2005), which can provide quantitative information on the likelihoods of different sets of parameters. The inversion results indicate that the most probable parameters characterizing the average seismic properties of the trapping structure, in the regions between the clusters of events indicated by the red and green stars and diamonds in Figs 8 and 10 and stations MMNB and FLIP, are velocity reductions of 30–40 per cent, Q values of 10–40, widths of about 140–160 m and depths of 3–4 km.

The inferred shallow depths of the local trapping structures below stations MMNB and FLIP are consistent with general expectations from rock mechanics studies, which indicate that increasing normal stress suppresses the damage generation (e.g. Jaeger & Cook 1979; Scholz 2002) and that it enhances strongly the healing process (e.g. Dieterich & Kilgore 1996; Johnson & Jia 2005). For these reasons, numerical simulations of zones sustaining irreversible deformation during earthquake failures produce generally flower-type structures with significant FZ damage limited to the shallow crust (Ben-Zion & Shi 2005; Ma 2008; Finzi *et al.* 2009). Some deep damage zones can be generated locally near persisting stepovers and other geometrical heterogeneities, but this is not a general characteristic of large sections of faults. The inferences on shallow FZ damage are consistent with the bulk of results associated with detailed analyses of seismic anisotropy (Cochran *et al.* 2003; Boness & Zoback 2004, 2006; Liu *et al.* 2004, 2005, 2008; Peng & Ben-Zion 2004, 2006) and analyses of temporal changes of seismic velocities (Peng & Ben-Zion 2006; Wu *et al.* 2009; Zhao & Peng 2009) around large faults and earthquake rupture zones. In fact, detailed analyses of data recorded in shallow boreholes and at the surface indicate that the material in the top ∼200 m of the crust has dominant effects on various signals associated with damaged FZ rocks (e.g. Liu *et al.* 2005; Rubenstein & Beroza 2005; Sawazaki *et al.* 2006; Chao & Peng 2009; Sleep 2009).

The diversity of results associated with our observations and modelling of trapped waves and phase delays implies a strongly variable FZ structure in the top few kilometres of the crust, with multiple discontinuous sections of damaged rocks rather than a continuous smoothly varying low velocity layer. This is consistent with detailed geological mapping, detailed analysis of site effects, detailed seismic tomography and detailed anisotropy studies along the Parkfield section of the SAF (e.g. Eberhart-Phillips & Michael 1993; Boness & Zoback 2004; Pitarka *et al.* 2006; Rymer *et al.* 2006; Liu *et al.* 2008), previous systematic analyses of trapped waves at Parkfield (Michael & Ben-Zion 1998; Korneev *et al.* 2003) and other locations (e.g. Peng *et al.* 2003; Mamada *et al.* 2004; Mizuno *et al.* 2004; Lewis *et al.* 2005) and detailed geological mappings of pulverized and damaged FZ rocks at various large FZs (e.g. Faulkner *et al.* 2003; Sibson 2003; Dor *et al.* 2006, 2008; Faulkner 2006; Mitchell & Faulkner 2009). There is also evidence for large scale variations of deeper FZ sections based on detailed analyses of head waves, *P* waves and relocated seismicity along several sections of the San Andreas and Calaveras faults (McGuire & Ben-Zion 2005; Lewis *et al.* 2007; Zhao & Peng 2008; Zhao *et al.* 2010) and detailed analysis of geodetic signals along the northern SAF (Jolivet *et al.* 2009).

The results from our comprehensive analyses and the studies discussed above, on the relatively shallow and strong diversity of FZ damage layers, imply that it is generally not possible to extrapolate results on FZ damage obtained at one or a few sites to large fault sections. The properties of the heavily damaged top few hundred meters of the crust affect strongly seismic data of surface and shallow borehole instruments. This produces considerable challenges for obtaining with such data reliable estimates of damage parameters at depth. The general agreement between our results and other studies on the strong velocity reduction (30–50 per cent) and low Q values (10–40) of the shallow seismic trapping structures can be used to constrain the rheologies and model parameters governing the damage and healing of shallow FZ rocks.

ACKNOWLEDGMENTS

The seismograms used in this study were recorded by the High Resolution Seismic Network (HRSN) operated by the Berkeley Seismological Laboratory, University of California, Berkeley, the Northern California Seismic Network (NCSN) operated by the U.S. Geological Survey, Menlo Park, the Parkfield Area Seismic Observatory (PASO) Network (Thurber *et al.* 2003) and the 2004 Parkfield guided wave experiment (Michael *et al.* 2005). We thank the various scientists involved with recording and making the data available, and Zhigang Peng, Peng Zhao and Zheqiang Shi for help with the data organization and discussions. The study was supported by the National Science Foundation (grant EAR-0844103). The paper benefited from comments by two anonymous referees and Editor Massimo Cocco.

REFERENCES

Ampuero, J.-P. & Ben-Zion, Y., 2008. Cracks, pulses and macroscopic asymmetry of dynamic rupture on a bimaterial interface with velocity-weakening friction, *Geophys. J. Int.,* **173**(2), 674–692, doi:10.1111/j.1365-246X.2008.03736.x.

Bakun, W.H. & Lindh, A.G., 1985. The Parkfield, California, earthquake prediction experiment, *Science,* **229,** 619–624.

Bakun, W.H. *et al*., 2005. Implications for prediction and hazard assessment from the 2004 Parkfield earthquake, *Nature,* **437,** 969–974.

Benites, R., Aki, K. & Yomogida, K., 1992. Multiple scattering of SH waves in 2-D media with many cavities, *Pure appl. Geophys.,* **138,** 353–390.

Ben-Zion, Y., 1989. The response of two joined quarter spaces to SH line sources located at the material discontinuity interface, *Geophys. J. Int.,* **98,** 213–222.

Ben-Zion, Y., 1990. The response of two half spaces to point dislocations at the material interface, *Geophys. J. Int.,* **101,** 507–528.

Ben-Zion, Y., 1998. Properties of seismic fault zone waves and their utility for imaging low velocity structure, *J. geophys. Res.,* **103,** 12 567–12 585.

Ben-Zion, Y. & Aki, K., 1990. Seismic radiation from an SH line source in a laterally heterogeneous planar fault zone, *Bull. seism. Soc. Am.,* **80,** 971–994.

Ben-Zion, Y. & Huang, Y., 2002. Dynamic rupture on an interface between a compliant fault zone layer and a stiffer surrounding Solid, *J. geophys. Res.,* **107**(B2), 2042, doi:10.1029/2001JB000254.

Ben-Zion, Y. & Malin, P., 1991. San Andreas fault zone head waves near Parkfield, California, *Science,* **251,** 1592–1594.

Ben-Zion, Y., Katz, S. & Leary, P., 1992. Joint inversion of fault zone head and direct P arrivals for crustal structure near major faults, *J. geophys. Res.,* **97,** 1943–1951.

Ben-Zion, Y. *et al*., 2003. A shallow fault zone structure illuminated by trapped waves in the Karadere-Duzce branch of the north Anatolian Fault, Western Turkey, *Geophys. J. Int.,* **152,** 699–717.

Ben-Zion, Y. & Shi, Z., 2005. Dynamic rupture on a material interface with spontaneous generation of plastic strain in the bulk, *Earth planet. Sci. Lett.,* **236,** 486–496, doi:10.1016/j.epsl.2005.03.025.

Boness, N.L. & Zoback, M.D., 2004. Multi-Scale Crustal Seismic Anisotropy in the Region Surrounding the San Andreas Fault Near Parkfield, CA, *EOS, Trans. Am. geophys. Un.,* **85**(47), Fall Meet. Suppl., Abstract T11F-05.

Boness N.L. & Zoback, M.D., 2006. A multiscale study of the mechanisms controlling shear velocity anisotropy in the San Andreas Fault Observatory at Depth, *Geophysics,* **71,** doi:10.1190/1.2231107.

Brietzke, G.B., Cochard, A. & Igel, H., 2009. Importance of bimaterial interfaces for earthquake dynamics and strong ground motion, *Geophys. J. Int.,* **178**(2), 921–938.

Brown R.D. *et al*., 1967. The Parkfield-Cholame California, earthquakes of June-August 1966—surface geologic effects water-resources aspects, and preliminary seismic data, *U.S. Geol. Surv.Profess. Paper,* **579,** 1–66.

Chao, K. & Peng, Z., 2009. Temporal changes of shear wave velocity and anisotropy in the shallow crust induced by the 10/22/1999 M6.4 Chia-Yi, Taiwan, earthquake, *Geophys. J. Int.,* **179,** 1800–1816, doi:10.1111/j.1365-246X.2009.04384.x.

Cochran, E.S., Vidale, J.E. & Li, Y.-G., 2003. Near-fault anisotropy following the Hector Mine earthquake, *J. geophys. Res.,* **108**(B9), 2436, doi:10.1029/2002JB002352.

Dieterich, J.H. & Kilgore, B.D., 1996. Imaging surface contacts: power law contact distributions and contact stresses in quartz, calcite, glass and acrylic plastic, *Tectonophysics,* **256,** 219–239.

Dor, O., Rockwell, T.K. & Ben-Zion, Y., 2006. Geologic observations of damage asymmetry in the structure of the San Jacinto, San Andreas and Punchbowl faults in southern California: A possible indicator for preferred rupture propagation direction, *Pure appl. Geophys.,* **163,** 301–349, doi:10.1007/s00024-005-0023-9.

Dor, O., Yildirim, C., Rockwell, T.K., Ben-Zion, Y., Emre, O., Sisk, M. & Duman, T.Y., 2008. Geologic and geomorphologic asymmetry across the rupture zones of the 1943 and 1944 earthquakes on the North Anatolian Fault: possible signals for preferred earthquake propagation direction, *Geophys. J. Int.,* **173,** 483–504, doi:10.1111/j.1365-246X.2008.03709.x.

Eberhart-Phillips, D. & Michael, A.J., 1993. Three-dimensional velocity structure, seismicity, and fault structure in the Parkfield region, central California, *J. geophys. Res.,* **98,** 15 737–15 758.

Ellsworth, W. L. *et al*., 2007. Seismology inside the fault zone: Applications to fault-zone properties and rupture dynamics, *Scientific Drilling,* **1,** 84–87.

Faulkner, D.R., 2006. The Structure and Mechanics of Large Strike-Slip Faults from Field Observations, *Geophys. Res. Abstr.,* **8,** 06260.

Faulkner, D.R., Lewis, A.C. & Rutter, E.H., 2003. On the internal structure and mechanics of large strike-slip fault zones: field observations of the Carboneras fault in southeastern Spain, *Tectonophysics,* **367**(3–4), 235–251.

Finzi, Y., Hearn, E.H., Ben-Zion, Y. & Lyakhovsky, V., 2009. Evolution of structural properties and deformation patterns of strike-slip faults: Numerical simulations incorporating damage rheology, *Pure appl. Geophys.,* **166,** 1537–1573, doi:10.1007/s00024-009-0522-1.

Fohrmann, M., Igel, H., Jahnke, G. & Ben-Zion, Y., 2004. Guided waves from sources outside faults: an indication for shallow fault zone structure? *Pure appl. Geophys.,* **161,** 2125–2137.

Haberland, C. *et al*., 2003. Modelling of seismic guided waves at the Dead Sea Transform, *J. geophys. Res.,* **108**(B7), 2342, doi:10.1029/2002JB002309.

Hamiel, Y., Liu, Y., Lyakhovsky, V., Ben-Zion, Y. & Lockner, D., 2004. A visco-elastic damage model with applications to stable and unstable fracturing, *Geophys. J. Int.,* **159,** 1155–1165, doi:10.1111/j.1365-246X.2004.02452.x.

Igel, H., Ben-Zion, Y. & Leary, P., 1997. Simulation of SH and P-SV wave propagation in fault zones, *Geophys. J. Int.,* **128,** 533–546.

Igel, H., Jahnke, G. & Ben-Zion, Y., 2002. Numerical simulation of fault zone guided waves: accuracy and 3-D effects, *Pure appl. Geophys.,* **159,** 2967–2083.

Jaeger, J.C. & Cook, N.G.W., 1979. *Fundamentals of Rock Mechanics,* Chapman and Hall, London.

Jahnke, G., Igel, H. & Ben-Zion, Y., 2002. Three-dimensional calculations of fault-zone-guided waves in various irregular structures, *Geophys. J. Int.,* **151,** 416–426.

Johnson, P.A. & Jia, X., 2005. Nonlinear dynamics, granular media and dynamic earthquake triggering, *Nature,* **437,** 871–874.

Jolivet, R., Bürgmann, R. & Houlié, N., 2009. Geodetic exploration of the elastic properties across and within the northern San Andreas Fault zone, *Earth planet. Sci. Lett.,* **288,** 126–131, doi:10.1016/j.epsl.2009.09.014.

Jongmans, D. & Malin, P.E., 1995. Microearthquake S-wave observations from 0 to 1 km in the Varian well at Parkfield, California, *Bull. seism. Soc. Am.,* **85,** 1805–1820.

Korneev, V.A., Nadeau, R.M. & McEvilly, T.V., 2003. Seismological studies at Parkfield IX: Fault-Zone Imaging Using Guided wave attenuation, *Bull. Seism. Soc. Am.,* **93,** 1415–1426.

Lees, J.M. & Malin, P.E., 1990. Tomographic images of *P*-wave velocity variation at Parkfield, California, *J. geophys. Res.,* **95**(B13), 21 793–21 804.

Lewis, M.A., Peng, Z., Ben-Zion, Y. & Vernon, F.L., 2005. Shallow seismic trapping structure In the San Jacinto fault zone near Anza, California, *Geophys. J. Int.,* **162,** 867–881.

Lewis, M.A., Ben-Zion, Y. & McGuire, J.J., 2007. Imaging the deep structure of the San Andreas Fault south of Hollister with joint analysis of fault-zone head and direct *P* arrivals, *Geophys. J. Int.,* **169**, 1028–1042, doi:10.1111/j.1365-246X.2006.03319.x.

Li, Y.-G. & Leary, P.C., 1990. Fault zone trapped waves, *Bull. seism. Soc. Am.,* **80**(5), 1245–1271.

Li, Y.-G. & Malin, P.E., 2008. San Andreas Fault damage at SAFOD viewed with fault-guided waves, *Geophys. Res. Lett.,* **35,** L08304, doi:10.1029/2007GL032924.

Li, Y.-G. & Vernon, F.L., 2001. Characterization of the San Jacinto fault zone near Anza, California, by fault zone trapped waves, *J. geophys. Res.,* **106,** 30 671–30 688.

Li, Y.-G., Leary, P.C., Aki, K. & Malin, P.E., 1990. Seismic trapped modes in the Oroville and San Andreas fault zones, *Science,* **249,** 763–766.

Li, Y.G., Aki, K., Adams, D., Hasemi, A. & Lee, W.H.K., 1994. Seismic guided waves trapped in the fault zone of the Landers, California, earthquake of 1992, *J. geophys. Res.,* **99,** 11 705–11 722.

Li, Y.-G., Ellsworth, W.L., Thurber, C.H., Malin, P.E. & Aki, K., 1997. Fault-Zone guided waves from explosions in the San Andreas fault at Parkfield and Cienega valley, California, *Bull. seism. Soc. Am.,* **87,** 210–221.

Li, H., Zhu, L. & Yang, H., 2007. High-resolution structures of the Landers fault zone inferred from aftershock waveform data, *Geophys. J. Int.,* **171,** 1295–1307.

Liu, Y., Teng, T.L. & Ben-Zion, Y., 2004. Systematic analysis of shear wave splitting in the aftershock region of the 1999 Chi-Chi earthquake: Evidence for shallow anisotropic structure and lack of systematic temporal variations, *Bull. seism. Soc. Am.,* **94,** 2330–2347.

Liu, Y., Teng, T.L. & Ben-Zion, Y., 2005. Near-surface seismic anisotropy, attenuation and dispersion in the aftershock region of the 1999 Chi-Chi, earthquake, *Geophys. J. Int.,* **160,** 695–706.

Liu, Y., Zhang, H., Thurber, C. & Roecker, S., 2008. Shear wave anisotropy in the crust around the San Andreas fault near Parkfield: spatial and temporal analysis, *Geophys. J. Int.,* **172**(3), 957–970.

Lindh, A.G. & Boore, D.M., 1981. Control of rupture by fault geometry during the 1966 Parkfield earthquake, *Bull. seism. Soc. Am.,* **71,** 95–116.

Ma, S., 2008. A physical model for widespread near-surface and fault zone damage induced by earthquakes, *Geochem. Geophys. Geosyst.,* **9,** Q11009, doi:10.1029/2008GC002231.

Mamada, Y., Kuwahara, Y., Ito, H. & Takenaka, H., 2004. Discontinuity of the Mozumi–Sukenobu fault low-velocity zone, central Japan, inferred from 3-D finite-difference simulation of fault zone waves excited by explosive sources, *Tectonophysics,* **378,** 209–222.

Mavko, G.T., Mukherji, T. & Dvorkin, J., 1998. *The Rock Physics Handbook-Tools for Seismic Analysis in Porous Media,* Cambridge Univ. Press, New York.

Michael, A.J. & Ben-Zion, Y., 1998. Inverting fault zone trapped waves with genetic algorithm, *EOS, Trans. Am. geophys. Un.,* **79,** F584.

Michael, A.J., Ross, S.L. & Hamilton, J., 2005. Imaging the Cholame valley fault stepover with guided waves, *Seismol. Res. Lett.,* **76**(2), 228.

Michelini, A. & McEvilly, T.V., 1991. Seismological studies at Parkfield. I. Simultaneous inversion for velocity structure and hypocenters using cubic B-splines parameterization, *Bull. seism. Soc. Am.,* **81,** 524–552.

Mitchell, T.M. & Faulkner, D.R., 2009. The nature and origin of off-fault damage surrounding strike-slip fault zones with a wide range of displacements: A field study from the Atacama fault system, northern Chile, *J. Struc. Geol.,* **31,** 802–816.

Mizuno, T. & Nishigami, K., 2006. Deep structure of the Nojima fault, southwest Japan, estimated from borehole observation of fault-zone trapped waves, *Tectonophysics,* **417,** 231–247.

Mizuno, T., Nishigami, K., Ito, H. & Kuwahara, Y., 2004. Deep structure of the Mozumi–Sukenobu fault, central Japan, estimated from the subsurface array observation of fault zone trapped waves, *Geophys. J. Int.,* **159,** 622–642.

McGuire, J. & Ben-Zion, Y., 2005. High-resolution imaging of the Bear Valley section of the San Andreas Fault at seismogenic depths with fault-zone head waves and relocated seismicity, *Geophys. J. Int.,* **163,** 152–164, doi:10.1111/j.1365-246X.2005.02703.x.

Nishigami, K., 2000. Deep crustal heterogeneity along and around the San Andreas fault system in central California and its relation to the segmentation, *J. geophys. Res.,* **105**(B4), 7983–7998.

Peng, Z. & Ben-Zion, Y., 2004. Systematic analysis of crustal anisotropy along the Karadere-Düzce branch of the north Anatolian fault, *Geophys. J. Int.,* **159,** 253– 274, doi:10.1111/j.1365-246X.2004.02379.x.

Peng, Z. & Ben-Zion, Y., 2006. Temporal changes of shallow seismic velocity around the Karadere-Duzce branch of the north Anatolian fault and strong ground motion, *Pure appl. Geophys.,* **163,** 567–599, doi:10.1007/s00024-005-0034-6.

Peng, Z., Ben-Zion, Y., Michael, A.J. & Zhu, L.P., 2003. Quantitative analysis of seismic fault zone waves in the rupture zone of the Landers, 1992, California earthquake: evidence for a shallow trapping structure, *Geophys. J. Int.,* **155,** 1021–1041.

Pitarka, A., Collins, N., Thio, H.-K., Graves, R. & Somerville, P., 2006. Implications of Rupture Process and Site Effects in the Spatial Distribution and Amplitude of the Near-Fault Ground Motion From the 2004 Parkfield Earthquake, SMIP06 Seminar on Utilization of Strong-Motion Data, pp. 19–40.

Revenaugh, J., 2000, The relation of crustal scattering to seismicity in southern California, *J. geophys. Res.,* **105,** 25 403–25 422.

Rovelli, A., Caserta, A., Marra, F. & Ruggiero, V., 2002. Can seismic waves be trapped inside an inactive fault zone ? The case study of NoceraUmbra, central Italy, *Bull. seism. Soc. Am.,* **92,** 2217–2232.

Rubinstein, J.L. & Beroza, G.C., 2005. Depth constraints on nonlinear strong ground motion, *Geophys. Res. Lett.,* **32,** L14313, doi:10.1029/2005GL023189.

Rubinstein, J.L., Uchida, N. & Beroza, G.C., 2007. Seismic velocity reductions caused by the 2003 Tokachi-Oki earthquake, *J. geophys. Res.,* **112,** B05315, doi:10.1029/2006JB004440.

Rymer, M.J. *et al*., 2006. Surface fault slip associated with the 2004 Parkfield, California, earthquake, *Bull. seism. Soc. Am.,* **96**(4B), S11–S27.

Sawazaki, K., Sato, H., Nakahara, H. & Mishimura, T., 2006. Temporal change in site response caused by earthquake strong motion as revealed from coda spectral ratio measurement, *Geophys. Res. Lett.,* **33,** L21303, doi:10.1029/2006GL027938.

Scholz, C.H., 2002. *The Mechanics of Earthquakes and Faulting,* Cambridge University Press, Cambridge.

Sibson, R.H., 2003. Thickness of the seismic slip zone, *Bull. seism. Soc. Am.*, **93**(3) 1169–1178

Sieh, K.E., 1978. Slip along the San Andreas fault associated with the great 1857 earthquake, *Bull. seism. Soc. Am.,* **68**(6), 1731–1749.

Shi, Z. & Ben-Zion, Y., 2006. Dynamic Rupture on a bimaterial interface governed by slip-weakening friction, *Geophys. J. Int.,* **164,** doi:10.1111/j.1365-246X.2006.02853.x.

Simpson, R.W., Barall, M., Langbein, J., Murray, J.R. & Rymer, M.J., 2004. San Andreas Fault Geometry in the Parkfield, California, Region, *Bull. Seismol. Soc. Am.,* **96**(4B), S28–S37.

Sleep, N.H., 2009. Depth of Rock Damage from Strong Seismic Ground Motions near the 2004 Parkfield Mainshock, *Bull. Seis. Soc. Am.,* **99**(5), 3067–3076.

Thurber, C.H., Roecker, S., Roberts, K., Gold, M., Powell, L. & Rittger, K., 2003. Earthquake locations and three-dimensional fault zone structure along the creeping section of the San Andreas Fault near Parkfield, CA: Preparing for SAFOD, *Geophys. Res. Lett.,* **30,** doi:10.1029/2002GL016004.

Thurber, C.H., Zhang, H., Waldhauser, F., Hardebeck, J., Michael, A. & Eberhart-Phillips, D., 2006. Three-dimensional compressional wavespeed model, earthquake relocations, and focal mechanisms for the Parkfield, California, region, *Bull. seism. Soc. Am.,* **96**(4B), S38–S49, doi:10.1785/0120050825.

Waldhauser, F., Ellsworth, W.L., Schaff, D.P. & Cole, A., 2004. Streaks, multiplets, and holes: high-resolution spatio-temporal behavior of Parkfield seismicity, *Geophys. Res. Lett.,* **31,** L18608, doi:10.1029/2004GL020649.

Wang C-Y., Mooney, W.D., Ding, Z., Yang, J., Yao, Z. & Lou, H., 2009. Shallow seismic structure of Kunlun fault zone in northern Tibetan Plateau, China: implications for the 2001 *M*s8.1 Kunlun earthquake, *Geophys. J. Int.,* **177,** 978–1000, doi:10.1111/j.1365-246X.2009.04049.x.

Wu, C., Peng, Z. & Ben-Zion, Y., 2009. Non-linearity and temporal changes of fault zone site response associated with strong ground motion, *Geophys. J. Int.,* **176,** 265–278.

Wu, J., Hole, J.A., Snoke, J.A. & Imhof, M.G., 2008. Depth extent of the fault zone seismic waveguide: Effects of increasing velocity with depth, *Geophys. J. Int.,* **173,** 611–622.

Zhao, P. & Peng, Z., 2008. Velocity contrast along the Calaveras fault from analysis of fault zone head waves generated by repeating earthquakes, *Geophys. Res. Lett.,* **35,** L01303, doi:10.1029/2007GL031810.

Zhao, P. & Peng, Z., 2009. Depth extent of damage zones around the central Calaveras fault from waveform analysis of repeating earthquakes, *Geophys. J. Int.,***179,** 1817–1930, doi:10.1111/j.1365-246X.2009.04385.x.

Zhao, P., Peng, Z., Shi, Z., Lewis, M. & Ben-Zion, Y., 2010. Variations of the Velocity Contrast and Rupture Properties of M6 Earthquakes along the Parkfield Section of the San Andreas Fault, *Geophys. J. Int*., doi:10.1111/j.1365-246X.2009.04436.x.